Published in final edited form as:
Dev Cell. 2023 October 09; 58(19): 1847–1863.e12. doi:10.1016/j.devcel.2023.08.031.

A kinesin-1 adaptor complex controls bimodal slow axonal transport of spectrin in *Caenorhabditis elegans*

Oliver Glomb[1,+], **Grace Swaim**[1,2,+], **Pablo Munoz LLancao**[2], **Christopher Lovejoy**[2], **Sabyasachi Sutradhar**[3], **Junhyun Park**[1], **Youjun Wu**[4], **Sydney E. Cason**[6,7], **Erika L.F. Holzbaur**[6,8], **Marc Hammarlund**[1,4], **Jonathon Howard**[3,5], **Shawn M. Ferguson**[2], **Michael W. Gramlich**[9], **Shaul Yogev**[1,*]

[1]Department of Neuroscience, Yale School of Medicine, CT 06510

[2]Department of Cell Biology, Yale School of Medicine, CT 06510

[3]Department of Molecular Biophysics and Biochemistry, Yale University, CT 06510

[4]Department of Genetics, Yale School of Medicine, CT 06510

[5]Quantitative Biology Institute, Yale University, CT 06510

[6]Department of Physiology, University of Pennsylvania, Philadelphia, PA 19104

[7]Neuroscience Graduate Group, University of Pennsylvania, Philadelphia, PA 19104

[8]Pennsylvania Muscle Institute, University of Pennsylvania, Philadelphia, PA 19104

[9]Department of Physics, Auburn University, Auburn, AL 36832

Summary

An actin-spectrin lattice, the Membrane Periodic Skeleton (MPS), protects axons from breakage. MPS integrity relies on spectrin delivery via slow axonal transport, a process that remains poorly understood. We designed a probe to visualize endogenous spectrin dynamics at single axon resolution in vivo. Surprisingly, spectrin transport is bimodal, comprising fast runs and movements that are 100-fold slower than previously reported. Modeling and genetic analysis suggest that the two rates are independent, yet both require kinesin-1 and the coiled coil proteins UNC-76/FEZ1 and UNC-69/SCOC, which we identify as spectrin-kinesin adaptors. Knockdown of either protein led to disrupted spectrin motility and reduced distal MPS, and UNC-76 overexpression instructed excessive transport of spectrin. Artificially linking spectrin to kinesin-1 drove robust motility but

---

[*]Corresponding author and lead contact: shaul.yogev@yale.edu.
[+]Equal contribution
Author contributions
OG, GS and SY designed, performed and analyzed all nematode related experiments, designed the figures and wrote the manuscript. SS and JH assisted with data analysis. PML, CL and SMF performed the IP from HEK293T cells. JP transfected and imaged SPTBN1/FEZ1/SCOC in Cos7 cells. YW and MH generated the 7xspGFP11::MIRO-1 knock in strain. MG generated the simulations of cargo transport. SEC and EH performed the kinesin-1 activation assay.

Declaration of Interests
The authors declare no competing or financial interests that could have appeared to influence the work reported in this paper.

inefficient MPS assembly, whereas impairing MPS assembly led to excessive spectrin transport, suggesting a balance between transport and assembly. These results provide insight into slow axonal transport and MPS integrity.

One-Sentence Summary

Bimodal slow axonal transport, controlled by a kinesin-1 adaptor complex, delivers spectrin for formation of the axonal membrane periodic skeleton.

eTOC blurb:

How cytoskeletal proteins are delivered to axons is unclear. Glomb, Swaim et al. found that spectrin is delivered at two distinct rates to the membrane periodic skeleton of the distal axon and identified kinesin-1 and two conserved adaptor proteins as the core components of the spectrin transport packet.

Graphical Abstract

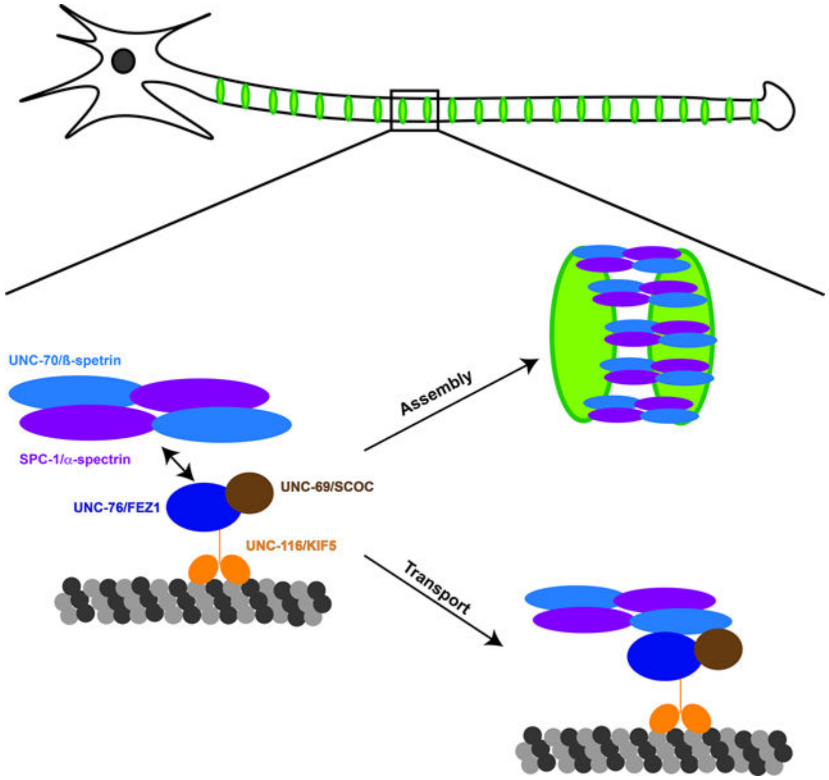

Introduction

A periodic lattice of actin rings and spectrin tetramers forms a Membrane associated Periodic Skeleton (MPS) that organizes the axonal membrane[1–3]. The MPS provides mechanical protection for the axon, is important for controlling its diameter, and organizes other transmembrane proteins into distinct functional domains[4–7]. Mutations in the MPS core component, spectrin, lead to a wide phenotypic spectrum, including axon breakage, synaptic instability, axonal degeneration, brain atrophy and Spinal Cerebellar Ataxia[8–14]. Despite its importance, the mechanisms that deliver spectrin to the axon to form or maintain the MPS are largely unknown.

Similar to other soluble and cytoskeletal proteins, spectrin is delivered to axons by slow transport[15–17], a poorly understood rate class defined by pulse chase radiolabeling studies[18–20]. Visualizing slow transport of individual cargo by fluorescence is highly challenging due to the ubiquitous nature of the cargo and its slow movement. Consequently, despite the importance of slow transport in delivering most axonal proteins, its mechanisms remain poorly understood compared to fast axonal transport, which delivers vesicular cargo[20,21].

Recent work using local photoactivation or photoconversion of tagged soluble and cytoskeletal cargo in cultured neurons began shedding light on slow transport mechanisms. Surprisingly, labeling cargo such as neurofilaments, microtubules, actin, dynein, synapsin or clathrin did not reveal processive slow movements but rather intermittent fast transport or biased diffusion underlined by fast transport[22–27]. Hence, current models suggest that the observed slow net movement in radiolabeling studies in fact represents intermittent fast motility, henceforth referred to as “stop-and-go”[20,25]. However, as many slow transport cargos have never been visualized directly or investigated mechanistically, additional mechanisms may exist.

We built a probe that allowed us to visualize the slow transport of α-spectrin at endogenous levels *in vivo*. We find that spectrin is delivered in two distinct slow transport modes: the previously described “stop-and-go” and an unexpected, 100-fold slower one, which we term “ultra-slow” and which is as processive as the fast runs in “stop and go” motility. We determined that kinesin-1 is the molecular motor responsible for both types of movements and identified UNC-76/FEZ1 and UNC-69/SCOC as a kinesin-spectrin adaptor module. Degradation of either protein drastically reduces spectrin transport and leads to elimination of the MPS from the distal axon and to age-dependent axonal degeneration. *In vitro*, both FEZ1 and SCOC are needed for kinesin-1 activation, and *in vivo,* UNC-69 and UNC-76 are required for each other’s levels and distribution. UNC-76 overexpression or disruption of MPS assembly in *unc-115/ablim/dematin* mutants increases transport at both rates, leading to distal accumulation of spectrin. Conversely, artificially linking spectrin to kinesin-1 yields rapid motility and only poorly rescues MPS loss in *unc-76* mutants. We suggest that axonal spectrin is in a balance between transport and assembly into the MPS, and speculate that it is transported with additional factors required for MPS formation.

Results

Spectrin distribution depends on kinesin-1

To address the mechanisms of spectrin axonal delivery *in vivo*, we used a previously validated split-GFP reporter system to restrict labelling of endogenous spectrin to a single axon[28]. This system consists of a 7xspGFP11 inserted in the endogenous *spc-1* locus (the sole *C. elegans* α-spectrin orthologue) and a spGFP1–10 expressed from cell-specific promoters. SPC-1::GFP was visualized in a cholinergic bipolar motor neuron, DA9, or in a touch receptor neuron, PLM (Figure 1A). DA9 is advantageous due to its mammalian-like axon/dendrite polarity, whereas the PLM major process has a wider caliber and thus holds more spectrin molecules, which increases SPC-1::GFP signal intensity and makes it amenable to STED (Stimulated Emission Depletion) imaging.

We tested whether SPC-1::GFP assembles into the MPS lattice using several assays. In PLM, where SPC-1::GFP intensity is high, 2D-STED was used to unambiguously visualize lattice periodicity (Figure 1D, E). Periodicity could also be visualized with SIM (Structured Illumination Microscopy), although it was less evident (Figure S1A–C), consistent with the lower resolution of this method. Next, we generated a β spectrin/UNC-70 single-cell knock down allele (referred to as *unc-70 scKD,* see methods for a description of degradation methods used in this study, UNC-70 is the only neuronal β spectrin in *C. elegans*) and observed a loss of periodicity in PLM (Figure 1D, E, S1B–C). In DA9, where the narrow caliber of the axon makes SPC-1::GFP less abundant, we could not use STED to resolve individual spectrin repeats. However, previous work showed MPS periodicity in DA9 using SIM[29], which we could confirm (Figure S1B). Furthermore, FRAP experiments, which were previously used to assess MPS integrity[30], showed that SPC-1::GFP was highly immobile in control DA9 axons but became mobile in *unc-70 scKD,* consistent with it being integrated into the MPS lattice (Figure S1D,E). Taken together, these data confirm previous results showing MPS periodicity in *C. elegans* and validate our ability to assay MPS integrity.

We next tested how mutations in kinesin motors – several of which co-precipitate with spectrin from mouse brain[10] – affect α-spectrin distribution. Mutations in kinesin-3/KIF1A (*unc-104(e1265)*) did not affect spectrin distribution (Figure S2A), whereas two mutant alleles of kinesin-1/KIF5, *unc-116(e2310)* and *unc-116(rh24sb79*) led to a strong reduction of the distal SPC-1::GFP signal (Figure S2B). Expression of *unc-116* cDNA in DA9 rescued spectrin distribution in *unc-116* mutants (Figure S2B) and cell-specific degradation of UNC-116 phenocopied *unc-116* mutants (Figure 1F, G, H), indicating that kinesin-1/KIF5 functions in DA9 to promote spectrin distribution.

unc-76/FEZ1 and *unc-69/SCOC* are required for spectrin distribution

To identify potential spectrin-kinesin adaptors, we tested mutations in the *C. elegans* orthologues of JIP1, JIP3 and kinesin light chains 1 and 2, but did not detect an effect on SPC-1::GFP distribution (Figure S2A). Conversely, we found that the conserved kinesin-1 binding protein UNC-76/FEZ1[31–34] was required for the distribution of SPC-1::GFP in the axon. SPC-1::GFP was strongly reduced in the distal axon upon single-cell degradation of UNC-76 (Figure 1B, C, F–H) or in the hypomorphic allele *unc-76 (e911)* (Figure S2E–F). We note that whereas *unc-76* mutants display axon guidance and fasciculation defects[32], *unc-76 scKD* animals showed normal axon guidance, suggesting that the axon-guidance function of *unc-76* is non-cell autonomous. We thus used primarily the *scKD* allele in subsequent experiments to avoid confounding effects from non-cell autonomous functions. Single cell degradation of UNC-76 reduced axon length (223 µm ±24 compared to 325 µm ±49 in wildtype, respectively) but no degeneration was observed in L4 animals (Figure S5) which is the stage in which we analyzed SPC-1::GFP distribution and spectrin transport. Degradation of UNC-76 only slightly enhanced SPC-1::GFP distribution defects in *unc-116* mutants, consistent with the two proteins functioning together and the two alleles not being complete nulls (Figure S2D).

Next, we tested how the strong reduction of distal SPC-1::GFP induced by UNC-76 degradation affects the MPS. In DA9, FRAP experiments suggested that the MPS was still assembled in the proximal axon where SPC-1::GFP is present (Figure S1E). To definitively test MPS integrity in *unc-76 scKD* animals we used STED in the PLM neurite. While the distal process lost the SPC-1::GFP signal (Figure 1B,C), the proximal region showed the expected MPS periodicity (Figure 1D,E). We conclude that *unc-76* is required for the formation of the distal MPS but not the proximal MPS, consistent with a role in spectrin transport.

To understand how UNC-76/FEZ1 functions, we tested whether any of its binding partners are required for MPS formation. We found that a single cell degradation allele of the poorly characterized short coiled-coil protein, UNC-69/SCOC[35–37], phenocopied the SPC-1::GFP misdistribution observed in *unc-76 scKD* (Figure 1F, G, H). Double degradation of both proteins only slightly enhanced the single degradation phenotypes, suggesting that both proteins function in the same genetic pathway (Figure S2D).

We next tested whether the function of UNC-76 and UNC-69 is conserved. We expressed cDNAs of human FEZ1 or SCOC in *unc-76* or *unc-69 scKD* animals, respectively, and found that both were able to restore the distribution of SPC-1::GFP in DA9 (Figure S2C). This result suggests that FEZ1 and SCOC can promote axonal delivery of spectrin.

FEZ1/UNC-76 and SCOC/UNC-69 cooperate to activate kinesin-1

To get further insight into how UNC-76 and UNC-69 function, we used CRISPR to tag both endogenous loci with a 10xspGFP11 or 7xspGFP11, respectively, and monitored their distribution in DA9. In control animals both proteins localize to the axon in a diffuse pattern (Figure 2A–B). Degradation of either UNC-76 or UNC-69 drastically reduced the axonal abundance of its partner (Figure 2A–F), suggesting that both proteins are interdependent for their axonal delivery. Consistent with Su et. al[35], we found that UNC-76 was dependent on kinesin-1 for its axonal delivery (Figure 2A, C, D).

To test whether UNC-76/FEZ1 and UNC-69/SCOC could link spectrin to kinesin-1 for axonal transport, we next examined whether SCOC and FEZ1, mammalian homologues of UNC-69 and UNC-76, co-migrate with spectrin and can physically interact with it. SPTBN1::GFP (human βII spectrin) was enriched near the plasma membrane when transfected in COS7 cells, while overexpressed FEZ1 and SCOC were mostly diffuse. Despite the diffuse background, we could also clearly detect SCOC, FEZ1 and SPTBN1 in puncta, consistent with the endogenous localization of FEZ1[33] (Figure S3A). ~70% of FEZ1 puncta contained SCOC, and ~20% contained both SCOC and SPTBN1 (Figure S3B). Furthermore, we observed motile puncta in which the three proteins co-migrated, suggesting that they reside in the same transport packet (Figure S3C,D). Consistent with these results, we co-immunoprecipitated HALO::SCOC and mCherry::FEZ1 with SPTBN1::GFP from transfected HEK293T lysates (Figure S3E,F). We conclude that SPTBN1, FEZ1 and SCOC are part of the same transport complex, although it is possible that additional proteins or vesicular intermediates exist between them.

Kinesin-1 is normally found in an inactive autoinhibited state, in which it shows very little microtubule binding[38–40]. To address the mechanism through which UNC-76/FEZ1 and UNC-69/SCOC promote kinesin-dependent spectrin delivery, we tested whether FEZ1 and SCOC promote kinesin-1 activation. We used TIRF microscopy to measure kinesin-1 binding on immobilized microtubules *in vitro*. In the presence of the non-hydrolysable ATP analog AMP-PNP (which keeps kinesin locked on the microtubule after binding), full length kinesin-1/KIF5B from lysed cell extracts showed little microtubule binding compared to KIF5B (1–560), which is not autoinhibited (Figure 2G–J). While either FEZ1 or SCOC on their own did not significantly increase microtubule binding, adding both proteins led to robust microtubule binding that was equivalent to the positive control KIF5B(1–560) (Figure 2H–J). These results suggest that FEZ1 and SCOC cooperate to activate kinesin-1 *in vitro,* consistent with their axonal localization interdependence *in vivo*.

Loss of *unc-76/FEZ1, unc-69/SCOC* and kinesin-1 affects multiple proteins associated with the MPS in multiple neurons

We next wondered whether the absence of SPC-1::GFP from the distal axon of neurons with compromised kinesin-1/UNC-76/UNC-69 activity is indicative of a broader reduction in proteins that can localize to the MPS. For this, we generated an endogenously tagged version of UNC-70/β-spectrin using the split-GFP labeling approach described earlier. GFP::UNC-70 was lost from the distal DA9 axon in *unc-69 scKD* and *unc-116 (e2310)* animals, similar to SPC-1::GFP (Figure 3A, B). Next, we visualized the MPS-associated protein Ankyrin/UNC-44 as a non-spectrin component of the lattice. We used a GFP insertion in the neuronal isoform of *unc-44*[41] and expressed pan-neuronal RFP as a ratiometric control. UNC-44::GFP was strongly reduced in *unc-76 (e911)* and *unc-116 (e2310)* mutants in regions where the DA9 axon is located, as well as in regions containing other axons along the dorsal nerve cord (Figure 3C,D). These results indicate that *unc-116*, *unc-76* and *unc-69* are required for the distribution of unc-70/ß-spectrin and unc-44/ Ankyrin.

The overall reduction of the broadly expressed UNC-44::GFP in *unc-76 (e911)* and *unc-116 (e2310)* mutants suggests that the function of these genes is not restricted to motor neurons (DA9) or touch receptor neurons (PLM). To evaluate this requirement with single cell resolution we examined SPC-1::GFP distribution in the glutamatergic interneuron PVQ and observed a strong distal reduction in *unc-76 (e911)* and *unc-116 (e2310)* mutants (Figure 3E,F). In contrast to these results, two other kinesin-1 cargos, mitochondria and RAB-11 vesicles, were not affected in *unc-76* mutants in DA9 (Figure S4). Taken together, these results indicate that *unc-76/FEZ1* and *unc-69/SCOC* are specifically required for the distribution of several MPS proteins in multiple neuronal classes of *C. elegans*.

Mutations in spectrin are associated with axon breakage and degeneration[8,11,42,43]. We asked whether loss of the MPS from the distal DA9 axon in *unc-76 scKD* animals would specifically cause distal axon degeneration. We visualized DA9 morphology with a cytosolic RFP and scored degenerating axons based on gaps in the RFP signal (Figure S5). Axonal gaps were rarely observed in L4 animals of either wildtype of *unc-76 scKD* animals, but by one day of adulthood a large fraction of *unc-76 scKD* animals displayed prominent distal axon degeneration as indicated by clear axon gaps and accompanied by swellings (Figure S5). We conclude that the distal absence of MPS proteins is associated with an early onset of distal axon degeneration.

Bimodal transport of spectrin

Since kinesin-1 functions in transport, and the distal loss of spectrin in the mutants is consistent with a transport defect, we next aimed to visualize spectrin transport. Fluorescent labeling of slow axonal transport cargo led to the model that slow transport in fact represents fast intermittent movements (“stop-and-go”[20,21]). Since tracking slow transport cargo *in vivo* at endogenous levels has not been previously done, we aimed to use our SPC-1 probe to test whether spectrin transport agrees with the above model. The high abundance of stationary spectrin in the MPS prevented us from using SPC-1::GFP to visualize the smaller fraction that is moving, even when using photobleaching (not shown). We therefore opted to genetically reproduce the pulse-chase approach of the original radiolabeling studies. We engineered an FRT-flanked termination sequence to separate the 7xspGFP11 tag from the C-terminus of endogenous *spc-1* to generate *spc-1$^{flip\text{-}on}$::GFP* (Figure 4A). We drove FLP expression from an integrated single-copy transgene with a heat shock promoter for temporal control of labeling and visualized SPC-1$^{\text{flip-on}}$::GFP specifically in the DA9 motor neuron by expressing spGFP1–10 with the *mig-13* promoter (Figure 4A). We optimized heat shock conditions to balance robust activation with minimal stress and tested a range of timepoints following activation (Figure S6A,B) to identify an imaging window where newly synthesized spectrin was sufficiently abundant to visualize yet not overly present in the immobile MPS fraction that masks the moving pool of molecules.

Strikingly, SPC-1$^{\text{flip-on}}$::GFP movement was different than described for other axonal cargo: instead of intermittent fast transport or biased diffusion, we observed a clear bimodal velocity distribution. On one end we detected ultra-slow runs (Figure 4B, D) that are ~100x slower than movements previously described using fluorescence. The speed of these runs (~0.009 μm/s or ~ 0.751 mm/day) and their anterograde bias match well with the results of radiolabeling experiments[16,17].

Consistent with a spectrin/UNC-76 transport complex, we could observe clear ultra-slow transport events for UNC-76::GFP, although the signal to noise ratio was much lower, since we did not have a temporal labeling control (Figure S6C).

At the other end, we could also detect a distinct, second rate-class of spectrin, which moved at ~0.63 μm/s and paused frequently, consistent with a “stop-and-go” model (Figure 4C, D)[20,44]. The processivity/run length of both rates was roughly similar (Figure 4E).

Since ultra-slow transport has not been previously observed by fluorescence, we aimed to test if it consists of fast intermittent movements, as postulated for other slow transport cargo[20,22,25]. First, we tripled our imaging rate from 30 sec/frame to 10 sec/frame and could still observe ultra-slow movements, suggesting this transport rate can be detected at multiple imaging frequencies (not shown). We note that at frame rates used for fast transport (10Hz), ultra-slow movement would result in a shift of ~1pixel/ 20 seconds, which is indistinguishable from noise. Next, we modeled axonal transport using a dynamic Mote Carlo approach (see methods) and asked whether fast instantaneous motility (stop-and-go) could explain the observed ultra-slow movement (Figure 4Fi). We found that fitting the fast instantaneous velocities observed for spectrin to an overall slow progression is theoretically possible but highly unlikely since it would require drastically restricting all runs (~90nm, roughly 11 kinesin-1 "steps"). (Figure 4Fii). The observed spectrin run-length measured using a high frame rate was significantly longer, and the observed pause duration was significantly shorter, than what would be required to account for ultra-slow transport under a "stop-and-go" model (Figure 4Fiii). We conclude that spectrin travels in at least two distinct rates, with the slower one being as processive (i.e., runs without stopping) as the faster one.

UNC-76/FEZ1 and UNC-116/kinesin-1 mediate bimodal spectrin transport

The distal loss of the MPS in *unc-116, unc-69* and *unc-76* mutants is suggestive of a defect in spectrin delivery, prompting us to visualize axonal transport progression in these mutants. We first tested whether the distribution of newly synthesized spectrin is shifted towards the cell body in the mutants, as would be expected from reduced transport. We averaged line-scans of axons from multiple animals per genotype at 8 hours after induction and observed a proximal shift in SPC-1$^{\text{flip-on}}$::GFP distribution in *unc-76 scKD* and *unc-116 (e2310)* mutants compared to wildtype (Figure 5A).

Next, we directly visualized spectrin motility over a one-hour imaging window and observed reduced ultra-slow transport in the anterograde direction (Figure 5B, C, D; a table of all transport quantifications is shown in Table S1), consistent with the role of kinesin in mediating anterograde transport in the axon. Similarly, faster imaging revealed a decrease of stop-and-go transport in the anterograde direction (Figure 5E, F). These results indicate that UNC-76 and kinesin-1 are required for both types of anterograde spectrin transport. Retrograde transport was less severely affected in the mutants (Table S1); however, the exclusive labelling of newly synthesized molecules by our probe leads to under-sampling of retrograde transport events, preventing us from drawing definitive conclusions about retrograde transport.

Our modeling indicates that stop-and-go and ultra-slow movements of spectrin represent distinct processes, while the genetic loss of function experiments suggest that both types of movements rely on the same core transport machinery. We therefore wondered whether we could identify additional genetic perturbations that would differentially affect each transport rate. Since opposite molecular motors often co-transport with a given cargo[45], we tested the effects of a dynein heavy chain/*dhc-1* mutation. A previously described temperature-sensitive lethal mutation H2157L in DHC-1 (identical to *dhc-1 (or195)*[46]) reduced anterograde ultra-slow transport frequency and mean velocity (Figure 5D, F), consistent with a some of the spectrin molecules moving faster and therefore not being detected at slow acquisition rate. In agreement, stop-and-go movements were slightly increased, although this increase was not statistically significant since the number of detected fast events exceeds that of slow events. Furthermore, we observed a differential requirement for β-spectrin's PH domain: a PH deletion mutant mildly reduced ultra-slow transport and mildly increased the number of stop-and-go SPC-1::GFP events (Figure 5D, F). Together, these results indicate that although both rates of spectrin movement require a shared core transport machinery, they are genetically separable.

Fast delivery of spectrin to the distal axon is not sufficient for MPS formation

Since our data indicate that UNC-76 links spectrin to kinesin-1, we reasoned that it could be replaced by an artificial tether between the two proteins. To test this, we expressed tagged kinesin light chain KLC-2 with an anti-GFP nanobody and injected this construct into *unc-76 scKD* animals expressing SPC-1::GFP (Figure 6A). In contrast to *unc-76 scKD* animals, in which spectrin transport is drastically reduced, KLC-2::nanobody (KLC-2::vhhGFP4) expressing animals displayed robust fast movement of endogenous spectrin, indicating that linking spectrin to kinesin-1 can restore its motility (Figure 6C). Interestingly, the KLC-2::nanobody construct only generated fast and processive spectrin movement, whereas slow movement (either “stop-and-go” or “ultra-slow”) was not restored (Figure 6D).

The exclusively rapid motility of spectrin induced by the artificial spectrin-kinesin-1 tether allowed us to ask whether rapid delivery of spectrin is sufficient to promote MPS formation in the distal axon. Compared to a control construct, the KLC-2::nanobody only restored the proximal-most ~20 μm out of the ~100 μm of steady-state SPC-1::GFP that are missing in *unc-76 scKD* animals (Figure 6A, B). Thus, although this rescue is statistically significant, its inefficiency highlights functional differences between rapid and slow axonal delivery mediated by UNC-76, with the latter potentially containing additional factors that promote its steady state distribution to the distal axon.

A balance between spectrin transport and MPS assembly

Last, we wondered whether the processes of spectrin transport and its assembly into the MPS are coordinated. For this we sought a mutation that would affect MPS assembly in *C. elegans.* The spectrin/actin crosslinker Dematin was recently shown to be an MPS component that is required for MPS assembly in cultured hippocampal neurons[47]. We tagged the endogenous locus of the *C. elegans* Dematin ortholog UNC-115 and tested if its localization PLM. Consistent with the localization of mammalian Dematin, GFP::UNC-115 showed the expected periodicity of an MPS associated protein in PLM (Figure S7B). Next, we tested GFP::SPC-1 distribution using STED in *unc-115 (ky275)* mutants and observed loss of MPS periodicity (Figure S7A,C). Together, these results indicate that UNC-115 is a functional homologue of Dematin and is required for MPS assembly.

To evaluate how defects in MPS assembly affect spectrin transport, we acquired movies of SPC-1$^{\text{flip-on}}$::GFP at high and low frame rates in *unc-115* mutants. Surprisingly, both ultra-slow and stop-and-go motility were significantly increased in *unc-115* mutants compared to wildtype (Figure 7C,D), suggesting that defects in MPS assembly lead to excessive spectrin transport. Furthermore, the increased spectrin motility in *unc-115* mutants was accompanied by an accumulation of SPC-1::GFP at the tip of the axon (Figure 7A), consistent with an imbalance in transport. To test whether this accumulation is indeed due to excessive anterograde transport we crossed *unc-115* mutants to *unc-76 scKD.* Degradation of UNC-76 eliminated the ectopic spectrin accumulation at the tip of the axon of *unc-115* mutants, confirming that this accumulation was due to excessive anterograde transport (Figure 7A).

As a second means of increasing spectrin transport, we overexpressed UNC-76 and UNC-69 in DA9. While UNC-69 overexpression had little effect (not shown), overexpression of RFP::UNC-76 led to an ectopic accumulation of SPC-1::GFP at the tip of the axon (Figure 7Bi), which was highly reminiscent of the accumulation in *unc-115* mutants. Spectrin enrichment correlated with the accumulation of UNC-76, suggesting that UNC-76 can instruct spectrin transport (Figure 7Bii). A control kinesin-1 cargo, MIRO-1::GFP, did not accumulate at the distal axon following UNC-76 overexpression (Figure 7Biii). Mutations in *unc-69* and *unc-116* eliminated the distal RFP::UNC-76 and SPC-1::GFP accumulations (not shown), consistent with the effect of these mutations on endogenous UNC-76 (Figure 2). Furthermore, in *unc-116* mutants, RFP::UNC-76 and SPC-1::GFP co-localized in punctate structures in the cell body (Figure 7Biv), consistent with an assembled transport particle which fails to move.

Given the similar steady-state phenotype of *unc-115* mutants and UNC-76 overexpression, we tested whether overexpression of UNC-76 also affected both transport rates. Indeed, we observed a strong increase both in ultra-slow and stop-and-go motility upon UNC-76 overexpression (Figure 7C, D), consistent with the interpretation that UNC-76 is instructive for spectrin transport. Taken together, the similarity between the steady state accumulation of spectrin and its increased transport both in *unc-115* mutants and UNC-76 overexpressing animals suggests that spectrin transport and its assembly into the MPS lattice balance each other.

Discussion

How spectrin and other cytoskeletal proteins are delivered from the cell body is poorly understood. To a large extent, this reflects the technical challenges of visualizing slow transport[20,48]. By developing a conditional labeling approach for spectrin, we observed its slow transport in individual axons *in vivo* at endogenous levels. Our results indicate that spectrin travels at two distinct rates, one of which is 100-fold slower than previously described transport rates. Mechanistically, although the two rates can be distinguished genetically and by modeling, they share a conserved core transport complex: kinesin-1/UNC-116, FEZ1/UNC-76 and SCOC/UNC-69. Knocking down this machinery severely compromises transport and the distal MPS in PLM. The three proteins interact with each other and with spectrin, co-migrate with spectrin and can instruct ectopic spectrin localization. Last, the similarity between the effects of UNC-76 overexpression and loss of *unc-115* suggest transport of spectrin and MPS assembly balance each other.

Bimodal slow axonal transport of spectrin

Radiolabeling experiments defined several rate classes of axonal transport, often referred to as Fast, Slow component a and Slow component b[18,20,21,48]. While several cases exist of proteins which do not fall squarely into one speed[17] or whose speed can change with age[49–51], spectrin seems unique in its ability to travel at two completely distinct rates, suggesting that it forms a part of different complexes. Consistently, our modeling argues that it is highly unlikely that ultra-slow movement consists of fast intermittent runs. The dependency of ultra-slow, but not stop-and-go motility on dynein and on spectrin's PH domain further supports this idea. These results agree with radiolabeling experiments that found that transported spectrin could be biochemically separated into different fractions[16]. Future biochemical studies should clarify the molecular composition of each fraction.

Despite the phenomenon of slow transport being firmly established, its function remains mysterious – why are so many axonal proteins moving slowly by a machinery that is capable of fast movement? In the case of spectrin, replacing both its slow movement rates with fast transport via the KLC-2::nanobody construct only mildly restored spectrin localization to the distal axon. This raises the hypothesis that the slow transport of spectrin by UNC-76 and UNC-69 makes it more available for MPS assembly, possibly by incorporating additional factors in the transport packet. This hypothesis is consistent with the dramatic increase in slow transport that we observed when MPS assembly was compromised in *unc-115* mutants and with the notion that assembly and transport balance each other (suggested by the similarity of UNC-76 overexpression and *unc-115* mutant phenotypes). Since loss of *unc-115* and overexpression of UNC-76 increased both stop-and-go and ultra-slow transport, and the effects of *dhc-1* mutation and the PH domain deletion were statistically significant but not strong, the precise functional roles of each one of these slow transport modes remains to be elucidated.

Current models of slow transport suggest that the vectorial slow movement observed by radiolabeling reflects underlying fast transport, either in the form of "stop-and-go" or "dynamic recruitment"[23,25–27,52]. These models are also supported by *in vitro* studies of molecular motors, none of which moves as slowly as slow axonal transport[53]. Our finding of ultra-slow yet processive spectrin movement indicates that additional ways of generating slow movements exist and may be uncovered in the future.

A transport complex that mediates the slow transport neuronal spectrin

Slow axonal transport depends on molecular motors[19,21,54] and the assembly of the MPS depends on microtubules[30]. However, less is known about adaptors that mediate slow transport. We found that FEZ1/UNC-76 and SCOC/UNC-69 link spectrin to kinesin for slow transport. This interpretation is consistent with the steady state MPS phenotype of the mutants, their loss of spectrin transport, physical interactions with spectrin or previously described physical interactions between UNC-76/FEZ1 and UNC-69/SCOC or UNC-76 and kinesin-1[31,34,35]. *In vitro*, both FEZ1 and SCOC were needed to promote kinesin-1 activation, and *in vivo* UNC-69 and UNC-76 were required for maintaining each other's levels and axonal distribution. *unc-69* and *unc-116* were also required for overexpressed UNC-76's ability to instruct ectopic transport.

Our data suggests that in DA9 UNC-79 and UNC-69 specifically transport spectrin; however, in other neurons they were suggested to transport additional cargo[33,55–60]. This is expected as the overall number of adaptors is likely smaller than the overall number of cargo species. Furthermore, SCOC's ability to cooperate with FEZ1 to activate kinesin-1 *in vitro* is highly reminiscent of another adaptor – JIP1[31]. While in *C. elegans* JIP1 was not required for spectrin transport, this similarity suggests that the assembly of cargo-adaptor complexes is somewhat modular. Last, technical considerations may account for some discrepancy in assigning cargo to adaptors based on loss of function phenotypes *in vivo*. In particular, the severe axon guidance defects of *unc-76* and *unc-69* mutants can affect synapse positioning and are a confounding factor when assessing the subcellular distribution of cargo, which is the reason we used single cell degradation approaches throughout this study.

How can the same transport complex move at two strikingly different speeds? One possibility is that a slower, unidentified motor determines the speed of the slower spectrin pool. Examples in which a slower kinesin associates with a faster one to determine overall speeds have been described in *C. elegans* cilia or in DRG neurons[61,62]. A related hypothesis is that dynein is also part of the transport complex. Artificially linking kinesin and dynein to generate a tug-of-war can generate slow movement *in vitro*[63–65] and we observed that a mutation in *dhc-1* specifically reduced the flux of anterograde ultra-slow cargo. While this is consistent with a tug-of-war mechanism, additional work would be required to establish this scenario, particularly since ultra-slow transport could also be explained by additional mechanisms. For example, multiple interactions of the cargo may enhance the drag force on the motor-cargo complex[64,66] or post-translational modification may slow down motor activity[67].

Limitations of the study

Although our strategy to fluorescently label newly synthesized spectrin molecules with a conditional 7xspGFP11 tag allowed us to visualize spectrin transport, the signal to background ratio remains low due to the high abundance of stationary spectrin molecules. This does not affect measurements of speed, but can lead to some ambiguity in determining where runs start or end, thereby introducing variability in parameters such as run-length. In the future, combining conditional labeling approaches with HALO/SNAP tags that rely on organic dyes should help to improve the signal of slow axonal transport cargo. Furthermore, we have followed primarily the transport of SPC-1/α-spectrin, and thus future studies should examine the dynamics of UNC-70/β-spectrin.

Another limitation of the study is that by labelling the newly-synthesized spectrin molecules we are likely under-sampling the population of retrogradely moving molecules which probably consists of many unlabeled proteins. Different probe designs will be required to specifically label this population.

STAR Methods

Resource availability

Lead contact—Further information and requests for resources and reagents should be directed to and will be fulfilled by the Lead Contact: Shaul Yogev (shaul.yogev@yale.edu).

Materials availability—Plasmids and transgenic nematode strains generated in this study are available from the lead contact upon request.

Data and Code Availability—The code that was used to model spectrin transport is deposited at github and is publicly available. The according link is provided in the key resources table. Raw microscopy data and western blots reported in this paper will be shared by the lead contact upon request. Any additional information required to reanalyze the data reported in this paper is available from the lead contact upon request.

Experimental model and study participant details—In this paper we used the nematode *Caenorhabditis elegans* as an in vivo model and HEK293T and COS7 cells for cell culture work.

Method details

Strains and maintenance—Nematode strains were cultured on nematode growth medium plates that were seeded with OP50 bacteria. Animals were grown at 20°C unless indicated otherwise.

Strain collection—A detailed nematode strain collection is provided in the key resources table. Strains generated by Frøkjær-Jensen[68] and Chen[41] are indicated.

Gene-editing by CRISPR/Cas-9—All CRISPR based gene-editing experiments were carried out based on a recently updated protocol by the Mello Lab[69]. In brief, in a total injection mix of 20 µl, 0.5 µl Cas9 (*S. pyogenes* Cas9 3NLS, 10µg/µl, IDT# 1081058), 3.7 µg gRNA (1.85 µg/g for each RNA, if two different gRNAs were used), 900fmol dsDNA repair template or 2.2 µg of ssDNA repair template having 32–35bp homology arms and 800 ng PRF4::rol-6(su1006) plasmid was added as a selection marker[70]. Nuclease free water was added to a total volume of 20 µl. The gRNA was synthesized from ssDNA using the EnGen sgRNA Synthesis Kit, S. pygenes (NEB# E3322S) and subsequently purifying the gRNA using a Monarch RNA cleanup kit (NEB#T2040). In case of dsDNA as a repair template, the dsDNA was melted and subsequently cooled before adding to the mixture.

The mixture was centrifuged at 14.000 rpm for 2 min and 18 µl were transferred to a fresh reaction tube and placed on ice until injected. F1 non-rollers were genotyped to find heterozygous edited mutants and singled to get homozygotes. Homozygotes were genotyped and sent for sanger sequencing.

The alleles unc-70(syb1684[unc-70(1166R + AID + 1167D)]) (V) and unc-69 (syb2774[zf-1::7xGFP11::unc-69]) (III) were generated by SunyBiotech.

Miro-1(wp119[7xGFP11::miro-1]) (IV) was also generated based on the updated protocol by the Mello Lab[69] but altered in the above-described procedure by adding the tracrRNA (IDT# 1072532) and crRNA separately to the injection mix instead of adding a preassembled gRNA.

For the single copy insertion by CRISPR, the injection mix contained the plasmid pOVG19 as a repair template (100 ng/µl), without a melting/cooling step before addition, as well as pMA122 (10 ng/µl) and pCFJ-90 (2 ng/µl) as selection markers. The mix was injected into the EG8078 containing a ttTi5605 landing site. The P0 generation was singled and grew for 10 days at 20°C. Successful injected animals generated non-uncoordinated moving F1- offspring, in which the uncoordinated movement was rescued by either a successful inserted single copy insertion or the formation of an extrachromosomal array. F1 progenies containing the extrachromosomal array were distinguishable from their single-copy inserted siblings by expressing a red head marker and a heat-shock inducible counter selection cassette. To exclude those extrachromosomal array containing offspring and enrich for offspring containing the successful single-copy insertion, the nematodes were heat shocked for 2h at 34°C, recovered for 4 h at 20°C and moving, non-red head containing F1ś were picked, singled and genotyped. F2 progenies that were homozygous for the single copy insertion were sent for sanger sequencing. All gRNA targeting sites together with the genotyping primers are listed in table S2, repair templates in table S3.

Plasmids—Plasmids were generated by standard restriction and ligation reactions or by Gibson Assembly and confirmed by Sanger Sequencing. Sequences and plasmids are available upon request. pGH8 was a gift from Erik Jorgensen[71] (Addgene plasmid #19359; http://n2t.net/addgene:19359; RRID: Addgene_19359). SPTBN1 cDNA was acquired from the plasmid ß2-spectrin-HA using standard restriction and ligation procedures. ß2-spectrin-HA was a gift from Vann Bennett (Addgene plasmid #31070; http://n2t.net/addgene:31070; RRID:Addgene_31070). The plasmid pRF-4 was generated by the Ambros Lab[70], pGH8[71], pMA122[72] and pCFJ90[68] by the Jorgensen lab. Plasmids were injected at the following concentrations into *C. elegans*: pRF-4 (40 ng/μl), pGH8 (5 ng/μl), pOVG19 (100 ng/μl), pMA122 (10 ng/μl), pCFJ90 (2 ng/μl), pOVG26 (2.5 ng/μl), pOVG36 (20 ng/μl), pOVG43 (10 ng/μl), pOVG44 (10 ng/μl), pMR18 (20 ng/μl), pMR20 (10 ng/μl), pOVG63 (10 ng/μl), pOVG67 (25 ng/μl), pOVG70 (25 ng/μl), pOVG65 (25 ng/μl), pOVG56 (25 ng/μl), pMR13 (30 ng/μl). All plasmids that were used in this study are listed in the key resources table.

Heatshock activation to temporally control fluorescence labelling of SPC-1— Heatshock was carried out at 34°C for 30 min. in a water bath incubating the nematodes in a parafilm sealed petri dish with the nematodes close to the water. The animals were subsequently placed at 20°C until imaging.

Cell specific labeling—For cell-specific labeling of endogenous proteins we tagged proteins with split GFP11 (see above for CRISPR protocol, sgRNAs and repair templates) and expressed split GFP1–10 as multi copy extrachromosomal transgenes, integrated multi-copy arrays or single copy insertions (see strain table for details) driven by the following promoters.

DA9 neuron: itr-1 promoter, mig-13 promoter

PLM neuron: mec-17 promoter

PVQ neuron: sra-6 promoter

Pan-neuronal: rab-3 promoter

The same promoters were used for expression of transgenic rescue constructs (for example with FEZ1, SCOC or the KLC-2::nanobody) and fluorescently labeled proteins (for example RFP::UNC-76).

Cell specific degradation—We induced degradation of target proteins using either the ZF1-ZIF-1[73] or auxin inducible TIR system[74]. Both systems rely on tagging the protein of interest at the endogenous locus using CRISPR (see above for specific sgRNAs and repair templates) and overexpressing an E3-ligase that is specific for the tag in a cell-specific manner using one of the promoters mentioned under “cell specific labeling”.

i) Auxin induced single cell specific knock down: All auxin induced knock down experiments were performed by culturing the animals on plates that contain NGM supplemented with 1 mM Auxin (Alfa Aesar #A10556) and seeded with OP50.

Adult animals were allowed to lay eggs for 2h on Auxin containing plates. Subsequently, adult animals were removed and the plates were maintained at 20°C until the progeny reached L4 stage and were imaged, unless indicated otherwise. The knock down condition was compared to a control condition that did not induce a knock down. As a control, i) in animals that expressed the TIR1 F-box protein from an extrachromosomal array, animals that lost the extrachromosomal array but co-cultured on auxin plates with their siblings were imaged or ii) in animals that expressed TIR1 from an integrated array, animals were cultured on NGM plates lacking auxin as a control condition.

ii) Cell specific knock down by the ZF-1/ZIF-1 system: UNC-76 and UNC-69 were endogenously tagged with a ZF1 zinc finger domain, which is recognized by the cell-specifically expressed E3 ubiquitin ligase substrate-recognition subunit ZIF-1[73]. These animals were raised on standard NGM plates and examined as L4 larvae.

iii) Evaluation of knockdown efficiency: Since cell specific degradation only reduces target proteins in a subset of cells in the entire animal, it is not informative to assay degradation by western blot. In the case of UNC-69 we included a 7xspGFP11 tag with the ZF1 degradation tag and found that only 5.32 % (s.d. 4.4 %, n=9 animals) of the fluorescence signal remained upon ZIF-1 expression. However, because this method is not very sensitive and because of the concern that adding the 7xspGFP11 tag may reduce degradation efficiency, this approach was not used for other degraded proteins. Instead, we evaluated knockdown efficiency by comparing phenotypes to available hypomorphic alleles. For *unc-116::AID*, we verified that the knock down condition resulted in stalling of mitochondrial transport, as observed in *unc-116(e2310)*. Both *unc-116::AID* and *unc-70::AID* showed a clear uncoordinated movement upon knockdown, caused by their inability to correctly move backwards, which is similarly observed in loss-of-function alleles of those genes. The efficiency of UNC-76 knockdown was compared to the hypomorphic *unc-76 (e911)*. Other than the fact that cell specific knockdown did not cause axon misguidance, single cell degradation of UNC-76 in DA9 yielded phenotypes that were at least as strong as *unc-76 (e911)*.

Microscopy—For standard microscopy, the nematodes were mounted on a 2 % agarose pad and paralyzed in a droplet of 10 mM Levamisole diluted in M9.

Measuring animal length during development—To determine the animal length during development, adult animals were allowed to lay eggs for 30 min before removal.

Removal of the adult animals set the timepoint 0 and animals were taken for imaging at 14h, 20h, 24h, 34h, 38h and 48h. Images were acquired on an upright LeicaDM4 B microscope equipped with a Leica MC170HD camera and a 10x air objective.

Fluorescence microscopy—Animals were imaged at larval stage L4 or as 1-day old adults. To image 1-day old adults, L4 larvae were synchronized at late L4 stage and then grown for additional 12 hours. For time-lapse recordings, the animals were first incubated in a droplet of 0.5 mM Levamisole diluted in M9 for 30 min and subsequently shifted into fresh M9 medium without paralytics onto a 10% agarose pad. Images were acquired with a Laser Safe DMi8 inverted microscope (Leica) equipped with a VT-iSIM system (BioVision) and an ORCA-Flash 4.0 camera (Hamamatsu) controlled by MetaMorph Advanced Confocal Acquisition Software Package. The microscope was equipped with an HC PL APO 63x/1.40NA OIL CS2, a HC PL APO 40x/1.30NA OIL CS2, a HC PL APO 20x/0.8NA AIR and HC PL APO 100x/1.47NA OIL objective as well as 488 nm, 561 nm and 637 nm laser lines.

Stimulated emission depletion (STED) microscopy—Animals were imaged at larval stage L4. Animals were mounted on a 2% agarose pad and paralyzed in a droplet of 10 mM Levamisole diluted in M9. Images were acquired on a Leica SP8 Gated STED 3xSuper Resolution microscope equipped with a tunable pulsed white laser (460nm- 660nm) for excitation, two PTM and two HyD detectors and a 100x objective/ 1.4 NA oil. For image acquisition, the white laser was tuned to 488nm excitation (70% total power) and coupled with a depletion laser at 592nm. The following acquisition parameter were used in all experimental conditions: 488nm laser intensity= 75%, Depletion Laser= 100%, Gating= 0.5–8, Line Average= 4, Frame Accumulation= 4. The microscope was controlled by the Leica LAS-X software and acquired images were deconvolved using the build in Huygens STED deconvolution software at default settings.

Quantification and statistical analysis

Fluorescence quantification—Raw images were processed and analyzed with Fiji/ImageJ v2.3.0/1.53f51[75,76]. Images were acquired as single layer or multiple layers and then stacked into maximum projections. To measure the signal intensity along the entire axon or animal, which could not be acquired in a single field of view, multiple images were taken and stitched into a single image using the pairwise-stitching plugin with a linear blending fusion method[77]. Time lapse microscopy images were stabilized with StackReg using the rigid body transformation method to correct for the movement or drift of animals during the recording time[78].

To calculate the signal intensity along a neurite, 5pxl thick lines were drawn along the length in the center of the neurite and a signal intensity profile was generated using the plot profile function.

The signal intensity was calculated as absolute signal intensities in arbitrary units as $I = I_{ROI} - I_{Background}$ or as relative intensity as $I = (I_{ROI1} - I_{Background})/(I_{ROI2} - I_{Background})$ as indicated in the figures, with $I_{Background}$ always being the background fluorescence of non-neuronal tissue next to the neuron. Kymographs were made using the Multi_kymograph plugin in ImageJ. For presentation purposes, some kymographs were background-subtracted using a rolling-ball, and the kymographs in Figure 7C and the insets of Figure 4B were background-subtracted using Fiji's FFT function. All kymograph analysis were performed before background subtractions.

Scoring axon degeneration—Axon degeneration was scored based on the discontinuity of a cytosolic RFP marker in the axon of DA9 in larval L4 animals as well as 1-day old adult animals.

Measuring lattice periodicity based on the autocorrelation function—Each data point in the autocorrelation amplitude plots corresponds to an average of three different regions that were randomly chosen along the length of the neurite in the field of view. A 1 pxl thick and 2 μm long line was drawn in ImageJ/FIJI to acquire an intensity profile. The autocorrelation function corresponding to each intensity profile was calculated with the acf function in R. To determine the amplitude of each autocorrelation function, the difference in f(x) of the first minimum and maximum were taken, with the restrictions that the first maximum had to occur before 340 nm for STED and 650 nm for SIM. For each neuron, the average of 3 amplitudes was determined.

Determining the spectrin signal coverage in the axon—To calculate the portion of the axon that contained SPC-1::GFP or GFP::UNC-70, fluorescence profiles along the center midline of the axon were acquired and the fluorescence intensity along the axon was normalized to the total fluorescence intensity. This intensity ratio was binned in 5 % intervals so that each interval should contain 5 % of the total signal intensity for a perfect homogenously distributed signal. The signal was considered as absent, when the signal intensity in an interval dropped below 2% and the intervals were summed up to this drop to determine the signal coverage. The length of the signal coverage in μm was determined by multiplying the signal coverage in % with the total length of the linescan.

Fluorescence recovery after photobleaching—Experiments were performed on a spinning disc confocal microscope (Olympus BX61) equipped with a Hamatsu C9100–50 camera and 405 nm, 488 nm and 561 nm laser lines and controlled by the software Volocity 2.0 (Quorum technologie).

The animals were prepared as just described for live cell imaging. A 2.41 μm×2.41 μm (10×10 pxl) large region of the axonal asynaptic zone was bleached using a 488nm laser, 57% laser intensity, 100 ms pulses in 60 cycles. controlled by a Perkin-Elmer photokinesis unit. 4–6 images were acquired before and 100 images were acquired after the photobleach in time intervals of 1 s of a single z-plane. To reduce acquisition bleach to a minimum, the signal intensity was binned by 2. Images were analyzed in Fiji/ImageJ and the intensity was measured by drawing a ROI i) in the region of interest, ii) in the shaft of the axon, as distant to the bleached region as possible, iii) in the background (non-neuronal tissue inside of the worm) and using the multi-measure function of Fiji. After subtracting the background signal (iii) from the intensity signal in the region of interest (i) as well as from the axon shaft (ii), a double normalization method was applied to determine the fluorescence intensity over time in the region of interest after photobleaching[79]:

$$I_i(t) = \frac{I_i(t)}{I_i(\text{prebleach})} \times \frac{I_{ii}(\text{prebleach})}{I_{ii}(t)}$$

with: I_i= signal intensity in the region of interest after background subtraction, I_{ii}= signal intensity in the axonal shaft after background subtraction and t= time. Intensity signals in each region from 4–6 images before the bleach were averaged to acquire I(prebleach). Animals which moved during the image acquisition were removed.

The FRAP curves were fitted in Graphpad Prism (version 7) using a one-phase association to determine the signal intensity at which the signal plateaued. FRAP curves that could not be fitted by a one-phase association because the confidence interval of the fit was unreliable, were excluded from the analysis. The mobile phase was calculated by subtracting the signal intensity at the first timepoint after bleaching (t_0) from the calculated plateaued signal intensity derived from a one phase association-fit of each curve $(mobile\ phase\ = I(plateau) - I(t_0))$.

Co-localization analysis—To quantitatively compare the co-localization between SPC-1::GFP and RFP::UNC-76 in wildtype, *unc-116(e2310)* and *unc-69 scKD* backgrounds, the ImageJ plugin “coloc 2” was used. The cell body in the green channel was encircled using the free hand selection tool and chosen as a ROI. Colocalization was scored based on the Pearson-correlation coefficient above Costes threshold to remove background signal by choosing the following parameter: Threshold regression by Costes, PSF=3 and Costes randomisations = 10.

Correlation in signal intensity enrichment at the distal DA9 tip—To determine the correlation between the signal enrichment of RFP::UNC-76 with either SPC-1::GFP or MIRO-1::GFP, the signal intensity at the distal DA9 tip was normalized to the signal intensity in the axonal shaft for either fluorescence channel. The obtained relative fluorescence enrichment at the axonal tip for each channel was correlated using a spearman-correlation.

Cell culture, transfection, and live cell imaging of COS7 cells—COS7 cells were cultured in DMEM containing 10% FBS, 1 mM sodium pyruvate, 100 U/ml penicillin, 100 mg/ml streptomycin, and 2 mM L-glutamine (all Gibco) in incubator maintained at 37°C and 5% CO_2. 48 hours prior to imaging experiments, cells were lifted with trypsin and plated on glass-bottomed dishes (MatTek) at a concentration of 70×10^3 cells per dish in DMEM without penstrep. 24 hours prior to imaging, cells were transfected with Lipofectamine 2000 (Invitrogen) in Opti-MEM (Gibco) for 2 hours. Just before imaging, Halo and SNAP tag ligands (JF549-HaloTag Ligand, JF646-SNAP tag ligand; kind gift from L. Lavis (Janelia Research Campus, Ashburn, VA)) were incubated at 1:10,000 concentration for 30 minutes. After the incubation, the imaging dish was gently washed with pre-warmed DMEM twice. Then the growth medium was replaced with live-cell imaging solution (Life Technologies). All live-cell imaging was performed at 37°C and 5% CO_2. Spinning-disk confocal microscopy was performed using an Andor Dragonfly system equipped with a plan apochromat objective (63×, 1.4 NA, oil) and a Zyla scientific CMOS camera. Detailed protocol for live cell imaging was deposited in protocols.io[80].

Immunoprecipitation of SPTBN1, FEZ1, and SCOC—HEK293T cells plated on 10-cm dishes were transiently transfected with 12 μg plasmids in two separate conditions: GFP (6 μg), Fez1-Cherry (3 μg), Scoc-Halo (3 μg), and βII-Spectrin (SPTBN1)-GFP (6 μg), FEZ1-Cherry (3 μg), SCOC-Halo (3 μg). Plasmids DNA were added to 500 μl Opti-MEM and 36 μl Fugene 6 transfection mix and incubated for 20 min before adding to the cells. After 48 h of transfection, cells were rinsed twice with cold PBS, lysed in cold lysis buffer (50 mM Tris, pH 7.4, 150 mM NaCl, and 1% Triton X-100) along with protease and phosphatase inhibitors (Complete Mini-EDTA free, PhosSTOP), and centrifuged at 14,000 rpm for 8 min at 4°C to collect the supernatant, leaving behind the insoluble pellet. For the immunoprecipitation, 5000 μg protein lysates were added to 25 μL of GFP-Trap beads (Chromotek) and incubated for 1 h at 4°C on a rotating shaker. Finally, the beads were washed five times with lysis buffer and eluted in 50 μl of 2× Laemmli buffer containing 1% 2-mercaptoethanol (Sigma-Aldrich) by heating at 95°C for 5 min.

For immunoblotting, protein samples were first separated on two gels. One gel to detect GFP and spectrin-GFP, and another gel to detect Fez1 and Scoc. For immunoblot, 10 μg of proteins lysate as input and 25 μl of immunoprecipitate were loaded per gel (4–12% gradient Mini-PROTEAN TGX precast polyacrylamide gels; Bio-Rad). After electrophoresis, samples were transferred to nitrocellulose membranes using a wet blot transfer system (Bio-Rad). The membranes were blocked with 5% nonfat dry milk prepared in TBST (Tris-buffered saline containing 0.1% Tween-20) for 1 h at room temperature followed by incubation with primary antibodies diluted in 5% Milk prepared in TBST at 4°C overnight. The antibodies used were anti-GFP (goat) peroxidase conjugated, 1:10000(Rockland, #600–103-215), Anti-RFP (Rabbit), 1:3000 (Rockland, #600–401-379), anti-HaloTag (Rabbit), 1:3000 (Promega, #G9211).

The next day, the membranes were washed 5 times with TBST and the membrane with Anti-Halo and Anti-RFP was incubated with anti-Rabbit HRP-conjugated secondary antibody 1:3000 (Cell signaling, #7074S) diluted in 5% nonfat dry milk in TBST for 1 h at room temperature. After secondary antibody incubation, the membrane was washed five times with TBST. Finally, the membranes were developed using SuperSignal™ West Pico PLUS Chemiluminescent Substrate (Thermo Fisher Scientific, # 34579) and SuperSignal™ West Femto Maximum Sensitivity Substrate (Thermo Fisher Scientific, # 34094) using a Chemidoc imaging system (Bio-Rad).

Kinesin-1 microtubule binding assay—COS-7 cells grown in 10 cm plates to 70–80% confluence expressing Halo-tagged K560 or KIF5B (KHC) were labeled with TMR 18–24 h post-transfection then lysed in P12 buffer (as described above) supplemented with 20 μM Taxol, 1 mM Mg-ATP, 0.1% Triton, and 10 μM DTT supplemented with protease inhibitors (described above). Separate plates expressing Halo- SCOC alone, FEZ1 alone, or SCOC and FEZ1 together were likewise lysed and labeled post-lysis with cell-impermeant Halo ligand AlexaFluor 660 (Promega). All lysates were clarified by a low speed (17000 × *g*) and a high speed (287582 × *g*) centrifugation. Flow chambers were assembled from a glass slide and a silanized (PlusOne Repel Silane, GE Healthcare) coverslip, held together by vacuum grease to form 10–15 μL volume chambers. A 1:40 dilution of monoclonal anti-tubulin antibody was flowed in and incubated 5 minutes. The chamber was then blocked with two 5 minute incubations of 5% pluronic F-127 (Sigma). Labeled (labeling ratio of 1:40, HiLyte 488, Cytoskeleton) Taxol-stabilized microtubules were then flowed into the chamber and immobilized on the antibody. Finally, diluted cell lysates were flowed in with P12 buffer containing 10 mM AMPPNP, 20 μM Taxol, 0.3 mg/ml bovine serum albumin, 0.3 mg/ml casein, 10 mM DTT, and an oxygen-scavenging system (0.5 mg ml^{-1} glucose oxidase, 470 U ml^{-1} catalase, and 3.8 mg ml^{-1} glucose). Videos were acquired using a Nikon TIRF microscopy system (Perkin Elmer, Waltham, MA) on an inverted Ti microscope equipped with a 100× objective and an ImageEM C9100–13 camera (Hamamatsu Photonics, Hamamatsu, Japan) with a pixel size of 0.158 μm and controlled with the program Volocity (Improvision, Coventry, England). Five microtubules per video were analyzed, taking care to avoid bundled microtubules. The mean fluorescence intensity of each microtubule was collected at 30 second intervals and normalized to K560 intensity at the final analyzed timepoint (4.5 minutes). Plots were generated and statistical analyses conducted in Prism 7.

Modeling of slow axonal transport—We model spectrin transport following our previously developed model approach for synaptic vesicle precursors using a dynamic Monte Carlo method in python[81]. In this study, spectrin transports on an axonal lattice with 4nm lattice size and 30 msec time-steps. The three different transport conditions (Fast, Fast+Pause, Slow) were modeled by setting cargo transport parameters (velocity, mean pause-time, detachment probability) at the beginning of each simulation. Briefly: (i) an individual simulated spectrin cargo speed was determined by a gaussian random number using the mean +/− stdev parameters for a given condition; (ii) at the beginning of each simulated time-step, an unweighted random number was generated to determine if the spectrin would detach from the lattice and end the simulation; (iii) if the spectrin follows the Fast+Pause model, then the cargo remained on the current lattice site if it was currently in a pause state; (iv) if not currently paused, the spectrin would then advance a set number of integer lattice sites determined by the velocity; (v) if the forward step is less than a whole integer lattice site, then the fractional step accumulates with the next time-step until a whole integer lattice site motion occurs. The simulation repeats steps (ii) – (v) until the cargo detaches and the simulation ends.

Aggregate simulated speed distributions, for comparison with experimental speed distributions, were calculated from individual simulations. The number of lattice sites traveled during the entire simulation was divided by the number of time-steps of the simulation and converted to microns/sec. Statistical difference was determined using two-tailed t-test on the individual simulated speeds for each condition (Fast, Fast+Pause, Slow). The data were then histogram binned with the same bin-sizes used for experimental data. Finally, cumulative distributions were calculated and compared for all simulated conditions and experimental data.

Statistical evaluation—Statistical evaluation was performed with GraphPad Prism (version 7). Each dataset was first tested for normality distribution by using the DÁgostino and Pearson test to judge the use of non- vs parametric statistical tests. Each test used in a given experiment as well as sample sizes are indicated in the figure or figure legend. When multiple comparisons were done, we used Dunn's correction for multiple comparisons (non-parametric) or Tukey's correction (parametric data). Violin plots show the median as well as the 25% and 75% quartiles. All correlation analysis is based on Spearman (non-parametric) or Pearson (parametric) correlation.

Supplementary Material

Refer to Web version on PubMed Central for supplementary material.

Acknowledgements

The authors would like to thank the Caenorhabditis Genetic Center (CGC) for sharing strains. This project is funded by the NIH grants R35-GM131744 (S.Y.) and AG062210 (S.M.F.), R01 NS118884 and NSF, PHY-2210464 (to J.H.) and R35 GM126950 (E.L.F.H). O.G. is supported by a Walter-Benjamin Scholarship funded by the Deutsche Forschungsgemeinschaft (DFG, German Research Foundation), Project# 465611822. We would like to thank the entire Yogev and Hammarlund labs for their technical assistance, feedback, and discussions. We would like to thank Martina Wirth and Sharon Tooze for providing us with FEZ1 and SCOC plasmids.

Inclusion and Diversity

We support inclusive, diverse, and equitable conduct of research.

References

1. D'Este E, Kamin D, Gottfert F, El-Hady A, and Hell SW (2015). STED nanoscopy reveals the ubiquity of subcortical cytoskeleton periodicity in living neurons. Cell Rep 10, 1246–1251. 10.1016/j.celrep.2015.02.007. [PubMed: 25732815]
2. Pielage J, Cheng L, Fetter RD, Carlton PM, Sedat JW, and Davis GW (2008). A presynaptic giant ankyrin stabilizes the NMJ through regulation of presynaptic microtubules and transsynaptic cell adhesion. Neuron 58, 195–209. 10.1016/j.neuron.2008.02.017. [PubMed: 18439405]
3. Xu K, Zhong G, and Zhuang X (2013). Actin, spectrin, and associated proteins form a periodic cytoskeletal structure in axons. Science 339, 452–456. 10.1126/science.1232251. [PubMed: 23239625]
4. Costa AR, Sousa SC, Pinto-Costa R, Mateus JC, Lopes CD, Costa AC, Rosa D, Machado D, Pajuelo L, Wang X, et al. (2020). The membrane periodic skeleton is an actomyosin network that regulates axonal diameter and conduction. Elife 9. 10.7554/eLife.55471.
5. Krieg M, Dunn AR, and Goodman MB (2014). Mechanical control of the sense of touch by beta-spectrin. Nat Cell Biol 16, 224–233. 10.1038/ncb2915. [PubMed: 24561618]
6. Wang T, Li W, Martin S, Papadopulos A, Joensuu M, Liu C, Jiang A, Shamsollahi G, Amor R, Lanoue V, et al. (2020). Radial contractility of actomyosin rings facilitates axonal trafficking and structural stability. J Cell Biol 219. 10.1083/jcb.201902001.
7. Zhou R, Han B, Xia C, and Zhuang X (2019). Membrane-associated periodic skeleton is a signaling platform for RTK transactivation in neurons. Science 365, 929–934. 10.1126/science.aaw5937. [PubMed: 31467223]
8. Hammarlund M, Jorgensen EM, and Bastiani MJ (2007). Axons break in animals lacking beta-spectrin. J Cell Biol 176, 269–275. 10.1083/jcb.200611117. [PubMed: 17261846]
9. Liu CH, and Rasband MN (2019). Axonal Spectrins: Nanoscale Organization, Functional Domains and Spectrinopathies. Front Cell Neurosci 13, 234. 10.3389/fncel.2019.00234. [PubMed: 31191255]
10. Lorenzo DN, Badea A, Zhou R, Mohler PJ, Zhuang X, and Bennett V (2019). betaII-spectrin promotes mouse brain connectivity through stabilizing axonal plasma membranes and

enabling axonal organelle transport. Proc Natl Acad Sci U S A 116, 15686–15695. 10.1073/pnas.1820649116. [PubMed: 31209033]

11. Miazek A, Zalas M, Skrzymowska J, Bogin BA, Grzymajlo K, Goszczynski TM, Levine ZA, Morrow JS, and Stankewich MC (2021). Age-dependent ataxia and neurodegeneration caused by an alphaII spectrin mutation with impaired regulation of its calpain sensitivity. Sci Rep 11, 7312. 10.1038/s41598-021-86470-1. [PubMed: 33790315]
12. Pielage J, Fetter RD, and Davis GW (2005). Presynaptic spectrin is essential for synapse stabilization. Curr Biol 15, 918–928. 10.1016/j.cub.2005.04.030. [PubMed: 15916948]
13. Pielage J, Fetter RD, and Davis GW (2006). A postsynaptic spectrin scaffold defines active zone size, spacing, and efficacy at the Drosophila neuromuscular junction. J Cell Biol 175, 491–503. 10.1083/jcb.200607036. [PubMed: 17088429]
14. Stankewich MC, Gwynn B, Ardito T, Ji L, Kim J, Robledo RF, Lux SE, Peters LL, and Morrow JS (2010). Targeted deletion of betaIII spectrin impairs synaptogenesis and generates ataxic and seizure phenotypes. Proc Natl Acad Sci U S A 107, 6022–6027. 10.1073/pnas.1001522107. [PubMed: 20231455]
15. Cheney R, Hirokawa N, Levine J, and Willard M (1983). Intracellular movement of fodrin. Cell Motil 3, 649–655. 10.1002/cm.970030529. [PubMed: 6198088]
16. Lorenz T, and Willard M (1978). Subcellular fractionation of intra-axonally transport polypeptides in the rabbit visual system. Proc Natl Acad Sci U S A 75, 505–509. 10.1073/pnas.75.1.505. [PubMed: 75548]
17. Willard M, Baitinger C, and Cheney R (1987). Translocations of fodrin and its binding proteins. Brain Res Bull 18, 817–824. 10.1016/0361-9230(87)90221-8. [PubMed: 3621001]
18. Black MM, and Lasek RJ (1980). Slow components of axonal transport: two cytoskeletal networks. J Cell Biol 86, 616–623. 10.1083/jcb.86.2.616. [PubMed: 6156946]
19. Miller KE, and Heidemann SR (2008). What is slow axonal transport? Exp Cell Res 314, 1981–1990. 10.1016/j.yexcr.2008.03.004. [PubMed: 18410924]
20. Roy S (2014). Seeing the unseen: the hidden world of slow axonal transport. Neuroscientist 20, 71–81. 10.1177/1073858413498306. [PubMed: 23912032]
21. Black MM (2016). Axonal transport: The orderly motion of axonal structures. Methods Cell Biol 131, 1–19. 10.1016/bs.mcb.2015.06.001. [PubMed: 26794507]
22. Ganguly A, Sharma R, Boyer NP, Wernert F, Phan S, Boassa D, Parra L, Das U, Caillol G, Han X, et al. (2021). Clathrin packets move in slow axonal transport and deliver functional payloads to synapses. Neuron 109, 2884–2901 e2887. 10.1016/j.neuron.2021.08.016. [PubMed: 34534453]
23. Scott DA, Das U, Tang Y, and Roy S (2011). Mechanistic logic underlying the axonal transport of cytosolic proteins. Neuron 70, 441–454. 10.1016/j.neuron.2011.03.022. [PubMed: 21555071]
24. Terada S, Kinjo M, Aihara M, Takei Y, and Hirokawa N (2010). Kinesin-1/Hsc70-dependent mechanism of slow axonal transport and its relation to fast axonal transport. EMBO J 29, 843–854. 10.1038/emboj.2009.389. [PubMed: 20111006]
25. Twelvetrees AE, Pernigo S, Sanger A, Guedes-Dias P, Schiavo G, Steiner RA, Dodding MP, and Holzbaur EL (2016). The Dynamic Localization of Cytoplasmic Dynein in Neurons Is Driven by Kinesin-1. Neuron 90, 1000–1015. 10.1016/j.neuron.2016.04.046. [PubMed: 27210554]
26. Wang L, and Brown A (2002). Rapid movement of microtubules in axons. Curr Biol 12, 1496–1501. 10.1016/s0960-9822(02)01078-3. [PubMed: 12225664]
27. Wang L, Ho CL, Sun D, Liem RK, and Brown A (2000). Rapid movement of axonal neurofilaments interrupted by prolonged pauses. Nat Cell Biol 2, 137–141. 10.1038/35004008. [PubMed: 10707083]
28. Jia R, Li D, Li M, Chai Y, Liu Y, Xie Z, Shao W, Xie C, Li L, Huang X, et al. (2019). Spectrin-based membrane skeleton supports ciliogenesis. PLoS Biol 17, e3000369. 10.1371/journal.pbio.3000369. [PubMed: 31299042]
29. He J, Zhou R, Wu Z, Carrasco MA, Kurshan PT, Farley JE, Simon DJ, Wang G, Han B, Hao J, et al. (2016). Prevalent presence of periodic actin-spectrin-based membrane skeleton in a broad range of neuronal cell types and animal species. Proc Natl Acad Sci U S A 113, 6029–6034. 10.1073/pnas.1605707113. [PubMed: 27162329]

30. Zhong G, He J, Zhou R, Lorenzo D, Babcock HP, Bennett V, and Zhuang X (2014). Developmental mechanism of the periodic membrane skeleton in axons. Elife 3. 10.7554/eLife.04581.
31. Blasius TL, Cai D, Jih GT, Toret CP, and Verhey KJ (2007). Two binding partners cooperate to activate the molecular motor Kinesin-1. J Cell Biol 176, 11–17. 10.1083/jcb.200605099. [PubMed: 17200414]
32. Bloom L, and Horvitz HR (1997). The Caenorhabditis elegans gene unc-76 and its human homologs define a new gene family involved in axonal outgrowth and fasciculation. Proc Natl Acad Sci U S A 94, 3414–3419. 10.1073/pnas.94.7.3414. [PubMed: 9096408]
33. Chua JJ, Butkevich E, Worseck JM, Kittelmann M, Gronborg M, Behrmann E, Stelzl U, Pavlos NJ, Lalowski MM, Eimer S, et al. (2012). Phosphorylation-regulated axonal dependent transport of syntaxin 1 is mediated by a Kinesin-1 adapter. Proc Natl Acad Sci U S A 109, 5862–5867. 10.1073/pnas.1113819109. [PubMed: 22451907]
34. Gindhart JG, Chen J, Faulkner M, Gandhi R, Doerner K, Wisniewski T, and Nandlestadt A (2003). The kinesin-associated protein UNC-76 is required for axonal transport in the Drosophila nervous system. Mol Biol Cell 14, 3356–3365. 10.1091/mbc.e02-12-0800. [PubMed: 12925768]
35. Su CW, Tharin S, Jin Y, Wightman B, Spector M, Meili D, Tsung N, Rhiner C, Bourikas D, Stoeckli E, et al. (2006). The short coiled-coil domain-containing protein UNC-69 cooperates with UNC-76 to regulate axonal outgrowth and normal presynaptic organization in Caenorhabditis elegans. J Biol 5, 9. 10.1186/jbiol39. [PubMed: 16725058]
36. Wirth M, Mouilleron S, Zhang W, Sjottem E, Princely Abudu Y, Jain A, Lauritz Olsvik H, Bruun JA, Razi M, Jefferies HBJ, et al. (2021). Phosphorylation of the LIR Domain of SCOC Modulates ATG8 Binding Affinity and Specificity. J Mol Biol 433, 166987. 10.1016/j.jmb.2021.166987. [PubMed: 33845085]
37. McKnight NC, Jefferies HB, Alemu EA, Saunders RE, Howell M, Johansen T, and Tooze SA (2012). Genome-wide siRNA screen reveals amino acid starvation-induced autophagy requires SCOC and WAC. EMBO J 31, 1931–1946. 10.1038/emboj.2012.36. [PubMed: 22354037]
38. Friedman DS, and Vale RD (1999). Single-molecule analysis of kinesin motility reveals regulation by the cargo-binding tail domain. Nat Cell Biol 1, 293–297. 10.1038/13008. [PubMed: 10559942]
39. Cai D, Hoppe AD, Swanson JA, and Verhey KJ (2007). Kinesin-1 structural organization and conformational changes revealed by FRET stoichiometry in live cells. J Cell Biol 176, 51–63. 10.1083/jcb.200605097. [PubMed: 17200416]
40. Kaan HY, Hackney DD, and Kozielski F (2011). The structure of the kinesin-1 motor-tail complex reveals the mechanism of autoinhibition. Science 333, 883–885. 10.1126/science.1204824. [PubMed: 21836017]
41. Chen F, Chisholm AD, and Jin Y (2017). Tissue-specific regulation of alternative polyadenylation represses expression of a neuronal ankyrin isoform in C. elegans epidermal development. Development 144, 698–707. 10.1242/dev.146001. [PubMed: 28087624]
42. Huang CY, Zhang C, Ho TS, Oses-Prieto J, Burlingame AL, Lalonde J, Noebels JL, Leterrier C, and Rasband MN (2017). alphaII Spectrin Forms a Periodic Cytoskeleton at the Axon Initial Segment and Is Required for Nervous System Function. J Neurosci 37, 11311–11322. 10.1523/JNEUROSCI.2112-17.2017. [PubMed: 29038240]
43. Huang CY, Zhang C, Zollinger DR, Leterrier C, and Rasband MN (2017). An alphaII Spectrin-Based Cytoskeleton Protects Large-Diameter Myelinated Axons from Degeneration. J Neurosci 37, 11323–11334. 10.1523/JNEUROSCI.2113-17.2017. [PubMed: 29038243]
44. Brown A (2000). Slow axonal transport: stop and go traffic in the axon. Nat Rev Mol Cell Biol 1, 153–156. 10.1038/35040102. [PubMed: 11253369]
45. Hancock WO (2014). Bidirectional cargo transport: moving beyond tug of war. Nat Rev Mol Cell Biol 15, 615–628. 10.1038/nrm3853. [PubMed: 25118718]
46. Hamill DR, Severson AF, Carter JC, and Bowerman B (2002). Centrosome maturation and mitotic spindle assembly in C. elegans require SPD-5, a protein with multiple coiled-coil domains. Dev Cell 3, 673–684. 10.1016/s1534-5807(02)00327-1. [PubMed: 12431374]
47. Zhou R, Han B, Nowak R, Lu Y, Heller E, Xia C, Chishti AH, Fowler VM, and Zhuang X (2022). Proteomic and functional analyses of the periodic membrane skeleton in neurons. Nat Commun 13, 3196. 10.1038/s41467-022-30720-x. [PubMed: 35680881]

48. Roy S (2020). Finding order in slow axonal transport. Curr Opin Neurobiol 63, 87–94. 10.1016/j.conb.2020.03.015. [PubMed: 32361600]

49. Hoffman PN, Lasek RJ, Griffin JW, and Price DL (1983). Slowing of the axonal transport of neurofilament proteins during development. J Neurosci 3, 1694–1700. [PubMed: 6192231]

50. Komiya Y (1980). Slowing with age of the rate of slow axonal flow in bifurcating axons of rat dorsal root ganglion cells. Brain Res 183, 477–480. 10.1016/0006-8993(80)90484-9. [PubMed: 6153285]

51. McQuarrie IG, Brady ST, and Lasek RJ (1989). Retardation in the slow axonal transport of cytoskeletal elements during maturation and aging. Neurobiol Aging 10, 359–365. 10.1016/0197-4580(89)90049-3. [PubMed: 2478905]

52. Rao AN, Patil A, Black MM, Craig EM, Myers KA, Yeung HT, and Baas PW (2017). Cytoplasmic Dynein Transports Axonal Microtubules in a Polarity-Sorting Manner. Cell Rep 19, 2210–2219. 10.1016/j.celrep.2017.05.064. [PubMed: 28614709]

53. Woehlke G, Ruby AK, Hart CL, Ly B, Hom-Booher N, and Vale RD (1997). Microtubule interaction site of the kinesin motor. Cell 90, 207–216. 10.1016/s0092-8674(00)80329-3. [PubMed: 9244295]

54. Baas PW, and Buster DW (2004). Slow axonal transport and the genesis of neuronal morphology. J Neurobiol 58, 3–17. 10.1002/neu.10281. [PubMed: 14598366]

55. Butkevich E, Hartig W, Nikolov M, Erck C, Grosche J, Urlaub H, Schmidt CF, Klopfenstein DR, and Chua JJ (2016). Phosphorylation of FEZ1 by Microtubule Affinity Regulating Kinases regulates its function in presynaptic protein trafficking. Sci Rep 6, 26965. 10.1038/srep26965. [PubMed: 27247180]

56. Chua JY, Ng SJ, Yagensky O, Wanker EE, and Chua JJE (2021). FEZ1 Forms Complexes with CRMP1 and DCC to Regulate Axon and Dendrite Development. eNeuro 8. 10.1523/ENEURO.0193-20.2021.

57. Fujita T, Maturana AD, Ikuta J, Hamada J, Walchli S, Suzuki T, Sawa H, Wooten MW, Okajima T, Tatematsu K, et al. (2007). Axonal guidance protein FEZ1 associates with tubulin and kinesin motor protein to transport mitochondria in neurites of NGF-stimulated PC12 cells. Biochem Biophys Res Commun 361, 605–610. 10.1016/j.bbrc.2007.07.050. [PubMed: 17669366]

58. Gunaseelan S, Wang Z, Tong VKJ, Ming SWS, Razar R, Srimasorn S, Ong WY, Lim KL, and Chua JJE (2021). Loss of FEZ1, a gene deleted in Jacobsen syndrome, causes locomotion defects and early mortality by impairing motor neuron development. Hum Mol Genet 30, 5–20. 10.1093/hmg/ddaa281. [PubMed: 33395696]

59. Huang PT, Summers BJ, Xu C, Perilla JR, Malikov V, Naghavi MH, and Xiong Y (2019). FEZ1 Is Recruited to a Conserved Cofactor Site on Capsid to Promote HIV-1 Trafficking. Cell Rep 28, 2373–2385 e2377. 10.1016/j.celrep.2019.07.079. [PubMed: 31422020]

60. Sure GR, Chatterjee A, Mishra N, Sabharwal V, Devireddy S, Awasthi A, Mohan S, and Koushika SP (2018). UNC-16/JIP3 and UNC-76/FEZ1 limit the density of mitochondria in C. elegans neurons by maintaining the balance of anterograde and retrograde mitochondrial transport. Sci Rep 8, 8938. 10.1038/s41598-018-27211-9. [PubMed: 29895958]

61. Gumy LF, Katrukha EA, Grigoriev I, Jaarsma D, Kapitein LC, Akhmanova A, and Hoogenraad CC (2017). MAP2 Defines a Pre-axonal Filtering Zone to Regulate KIF1- versus KIF5-Dependent Cargo Transport in Sensory Neurons. Neuron 94, 347–362 e347. 10.1016/j.neuron.2017.03.046. [PubMed: 28426968]

62. Snow JJ, Ou G, Gunnarson AL, Walker MR, Zhou HM, Brust-Mascher I, and Scholey JM (2004). Two anterograde intraflagellar transport motors cooperate to build sensory cilia on C. elegans neurons. Nat Cell Biol 6, 1109–1113. 10.1038/ncb1186. [PubMed: 15489852]

63. Belyy V, Schlager MA, Foster H, Reimer AE, Carter AP, and Yildiz A (2016). The mammalian dynein-dynactin complex is a strong opponent to kinesin in a tug-of-war competition. Nat Cell Biol 18, 1018–1024. 10.1038/ncb3393. [PubMed: 27454819]

64. DeBerg HA, Blehm BH, Sheung J, Thompson AR, Bookwalter CS, Torabi SF, Schroer TA, Berger CL, Lu Y, Trybus KM, and Selvin PR (2013). Motor domain phosphorylation modulates kinesin-1 transport. J Biol Chem 288, 32612–32621. 10.1074/jbc.M113.515510. [PubMed: 24072715]

65. Soppina V, Rai AK, Ramaiya AJ, Barak P, and Mallik R (2009). Tug-of-war between dissimilar teams of microtubule motors regulates transport and fission of endosomes. Proc Natl Acad Sci U S A 106, 19381–19386. 10.1073/pnas.0906524106. [PubMed: 19864630]
66. Hill DB, Plaza MJ, Bonin K, and Holzwarth G (2004). Fast vesicle transport in PC12 neurites: velocities and forces. Eur Biophys J 33, 623–632. 10.1007/s00249-004-0403-6. [PubMed: 15071760]
67. Banerjee R, Chakraborty P, Yu MC, and Gunawardena S (2021). A stop or go switch: glycogen synthase kinase 3beta phosphorylation of the kinesin 1 motor domain at Ser314 halts motility without detaching from microtubules. Development 148. 10.1242/dev.199866.
68. Frokjaer-Jensen C, Davis MW, Sarov M, Taylor J, Flibotte S, LaBella M, Pozniakovsky A, Moerman DG, and Jorgensen EM (2014). Random and targeted transgene insertion in Caenorhabditis elegans using a modified Mos1 transposon. Nat Methods 11, 529–534. 10.1038/nmeth.2889. [PubMed: 24820376]
69. Ghanta KS, and Mello CC (2020). Melting dsDNA Donor Molecules Greatly Improves Precision Genome Editing in Caenorhabditis elegans. Genetics 216, 643–650. 10.1534/genetics.120.303564. [PubMed: 32963112]
70. Mello CC, Kramer JM, Stinchcomb D, and Ambros V (1991). Efficient gene transfer in C.elegans: extrachromosomal maintenance and integration of transforming sequences. EMBO J 10, 3959–3970. [PubMed: 1935914]
71. Frokjaer-Jensen C, Davis MW, Hopkins CE, Newman BJ, Thummel JM, Olesen SP, Grunnet M, and Jorgensen EM (2008). Single-copy insertion of transgenes in Caenorhabditis elegans. Nat Genet 40, 1375–1383. 10.1038/ng.248. [PubMed: 18953339]
72. Frokjaer-Jensen C, Davis MW, Ailion M, and Jorgensen EM (2012). Improved Mos1-mediated transgenesis in C. elegans. Nat Methods 9, 117–118. 10.1038/nmeth.1865. [PubMed: 22290181]
73. Armenti ST, Lohmer LL, Sherwood DR, and Nance J (2014). Repurposing an endogenous degradation system for rapid and targeted depletion of C. elegans proteins. Development 141, 4640–4647. 10.1242/dev.115048. [PubMed: 25377555]
74. Zhang L, Ward JD, Cheng Z, and Dernburg AF (2015). The auxin-inducible degradation (AID) system enables versatile conditional protein depletion in C. elegans. Development 142, 4374–4384. 10.1242/dev.129635. [PubMed: 26552885]
75. Schindelin J, Arganda-Carreras I, Frise E, Kaynig V, Longair M, Pietzsch T, Preibisch S, Rueden C, Saalfeld S, Schmid B, et al. (2012). Fiji: an open-source platform for biological-image analysis. Nat Methods 9, 676–682. 10.1038/nmeth.2019. [PubMed: 22743772]
76. Schneider CA, Rasband WS, and Eliceiri KW (2012). NIH Image to ImageJ: 25 years of image analysis. Nat Methods 9, 671–675. 10.1038/nmeth.2089. [PubMed: 22930834]
77. Preibisch S, Saalfeld S, and Tomancak P (2009). Globally optimal stitching of tiled 3D microscopic image acquisitions. Bioinformatics 25, 1463–1465. 10.1093/bioinformatics/btp184. [PubMed: 19346324]
78. Thevenaz P, Ruttimann UE, and Unser M (1998). A pyramid approach to subpixel registration based on intensity. IEEE Trans Image Process 7, 27–41. 10.1109/83.650848. [PubMed: 18267377]
79. Phair RD, Gorski SA, and Misteli T (2004). Measurement of dynamic protein binding to chromatin in vivo, using photobleaching microscopy. Methods Enzymol 375, 393–414. 10.1016/s0076-6879(03)75025-3. [PubMed: 14870680]
80. Marianna Leonzino AG-S, De Camilli Pietro (2021). Cell culture, transfection and imaging. protocols.io. 10.17504/protocols.io.bvgmn3u6.
81. Gramlich MW, Balseiro-Gomez S, Tabei SMA, Parkes M, and Yogev S (2021). Distinguishing synaptic vesicle precursor navigation of microtubule ends with a single rate constant model. Sci Rep 11, 3444. 10.1038/s41598-021-82836-7. [PubMed: 33564025]

Highlights

- Visualization of two distinct axonal transport rates of α-spectrin
- FEZ1 and SCOC can form a complex with spectrin
- MPS components are lost from the distal axon of the transport-complex mutants
- spectrin transport and MPS assembly balance each other

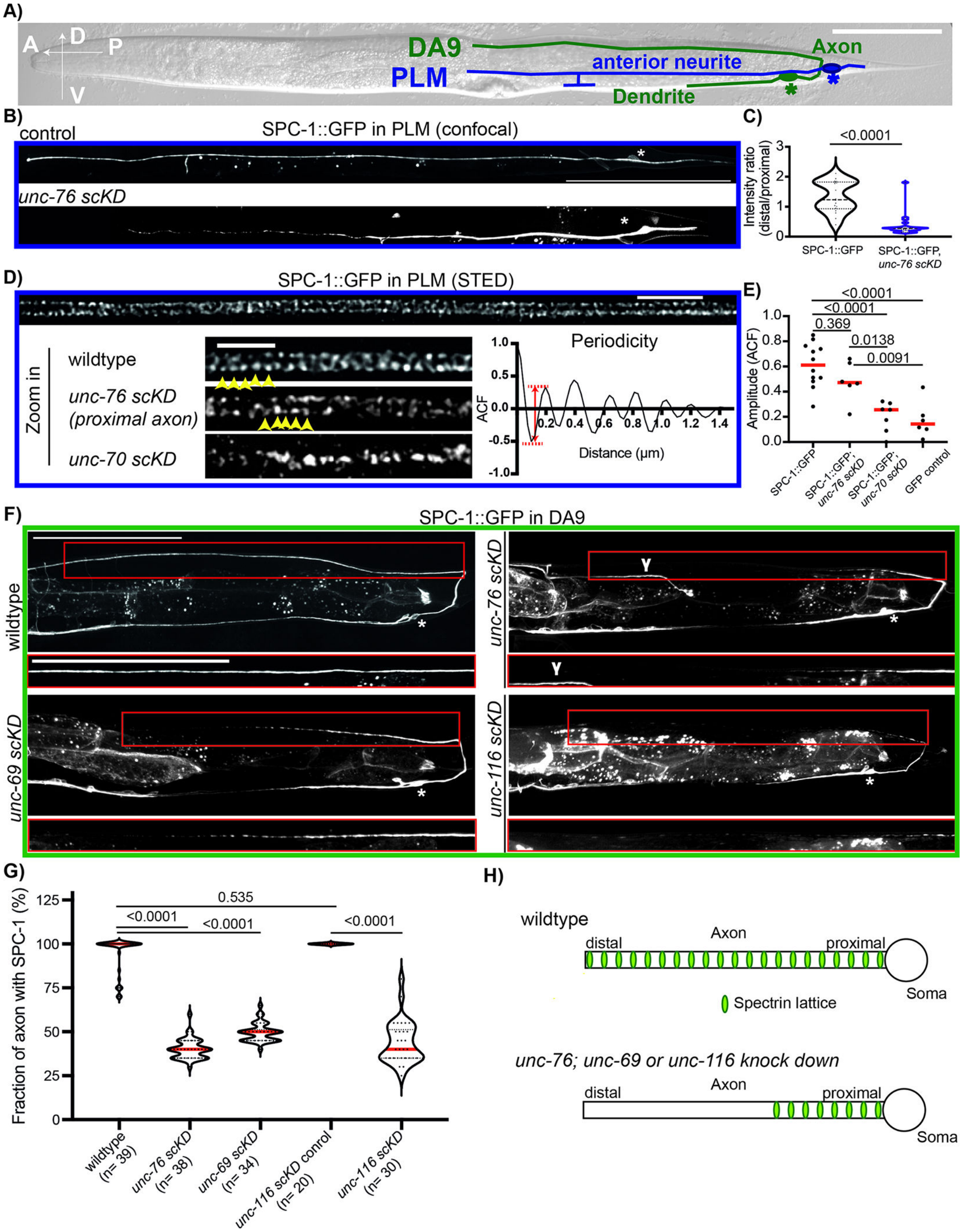

Figure 1: Kinesin-1/UNC-116, FEZ1/UNC-76 and SCOC/UNC-69 are required to distribute axonal spectrin.

A. Positions of DA9 (green) and PLM (blue) indicated on an image of *C. elegans*. Scale: 100 µm. **B.** Confocal images of endogenous α-spectrin/SPC-1 in PLM in control and *unc-76 single cell knock down (scKD)*. Scale: 100 µm. * indicates the cell body. **C.** Quantification of B, n= 18–25 animals per genotype, Mann-Whitney comparison. Violin plot indicates mean (bold) and 25th/75th percentiles (faint lines). **D.** Representative 2D-STED images of SPC-1::GFP in PLM in indicated genotypes. Yellow arrowheads point to individual spectrin repeats that show a periodicity of ~ 200 nm. Lower right panel shows quantification of periodicity by measuring the amplitude between the first minimum and maximum of an autocorrelation function (ACF). Scale=2 µm (overview image) or 1 µm (zoom). **E.** Comparison of periodicity of the genotypes shown in D and a soluble GFP control. n= 6–12 animals per genotype, 1-way ANOVA with Tukey's post-test for multiple comparisons. **F.** Representative confocal images of SPC-1::GFP in DA9 of wildtype or single-cell knock downs of *unc-116*, *unc-76* or *unc-69* show strong loss of spectrin signal in the axon, highlighted by boxes. Lower panels show the SPC-1 signal in the distal axon (proximal to distal from right to left). Y indicates SDQL neuron that is sometimes labeled by *mig-13* promoter. Scale: 100 µm. **G**. Quantification of F. *unc-116* control: animals raised without Auxin, which is required for degradation. N (animals) as indicated on graph with 20–39 animals per genotype. Kruskal-Wallis test followed by Dunńs post-test for multiple comparisons. **H**. Summary cartoon of spectrin distribution in wildtype and mutants.

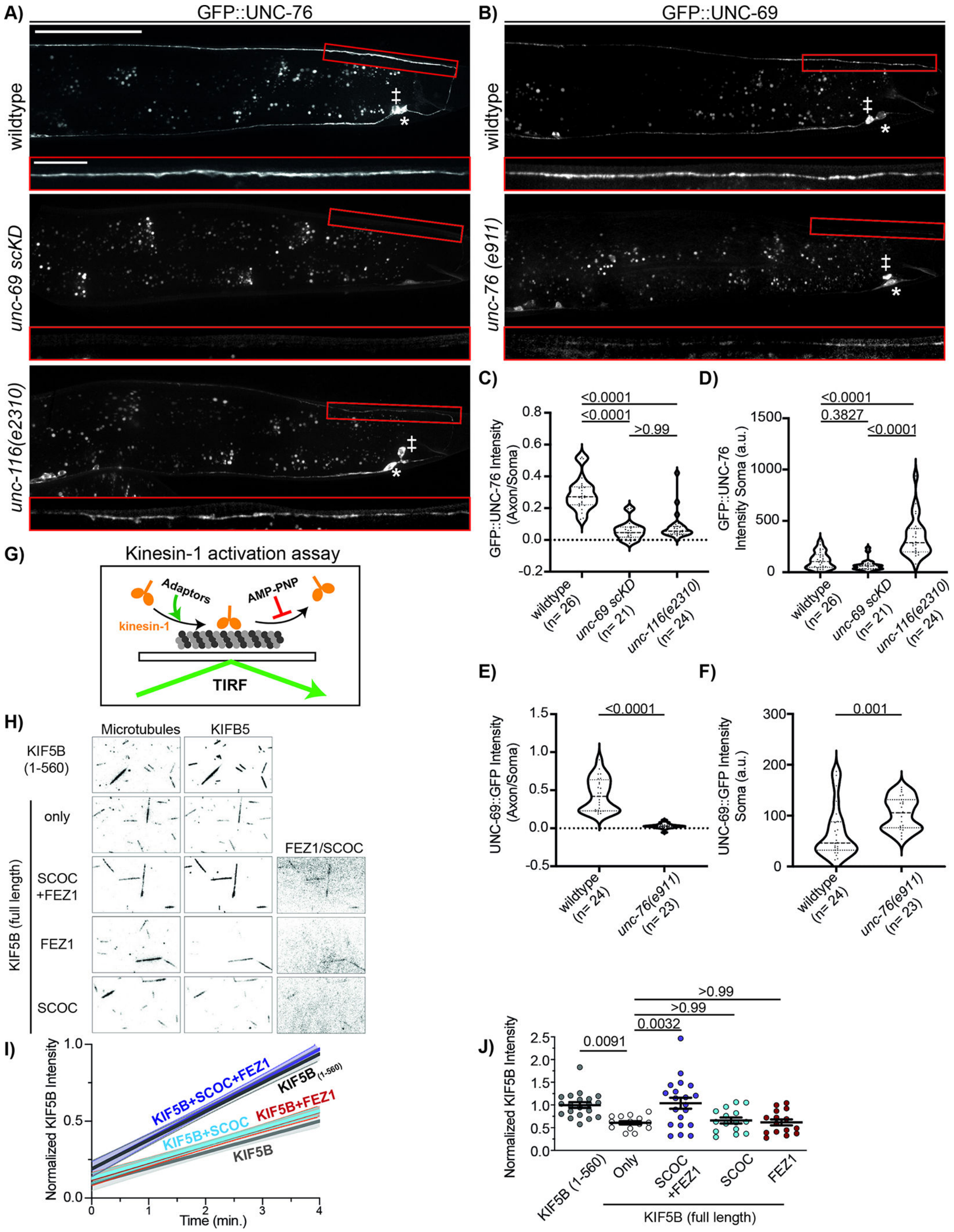

Figure 2: FEZ1/UNC-76 and SCOC/UNC-69 are interdependent for localization and activity. **A.** Endogenous UNC-76 (cell specifically labeled) localizes throughout the axon. Axonal levels of UNC-76 are drastically reduced in *unc-116 (e2310)* mutants and *unc-69 scKD.* **B**. Endogenously tagged UNC-69 localizes throughout the axon. UNC-69 levels are strongly reduced in *unc-76 (e911)* mutants. Boxed regions in A and B indicate the dorsal part of the DA9 axon. Asterisks mark the DA9 cell body. The cell body of VA12, which is also labelled by the *mig-13* promoter, is indicated with a ‡. Scale: 50 µm. **C, D**. Quantification of GFP::UNC-76 distribution (C) and signal intensity in the soma (D) of the strains shown

in A. Kruskal-Wallis test followed by Dunńs post-test for multiple comparisons. n= 21–26 animals per genotype. **E, F**. Quantification of the UNC-69::GFP signal distribution as in C+D but with the strains shown in B. n=23–24 animals per genotype. Mann-Whitney test for comparison. **G.** Schematic of the kinesin-1 recruitment to microtubules assay. The non-hydrolysable ATP analog AMPPNP prevents activated kinesin-1 dissociation from microtubules, allowing to measure kinesin accumulation following activation by FEZ1/SCOC. **H.** FEZ1 and SCOC synergistically activate the recruitment of kinesin-1 (KHC5B) to microtubules. Representative TIRF images showing fluorescently labeled microtubules, kinesin-1 (KIF5, either truncated 1–560 motor domain or full-length), and SCOC and/or FEZ1 (same channel) after 270s. **I.** Linear regression (95% confidence interval) of KIF5 recruitment to the microtubules over time. Mean intensity values were normalized to the average maximum intensity of K560 (for that trial). **J.** Quantification of KIF5 recruitment at timepoint 270s. n = 15–20 microtubules each from 4 trials; one-way ANOVA with Tukey’s multiple comparisons.

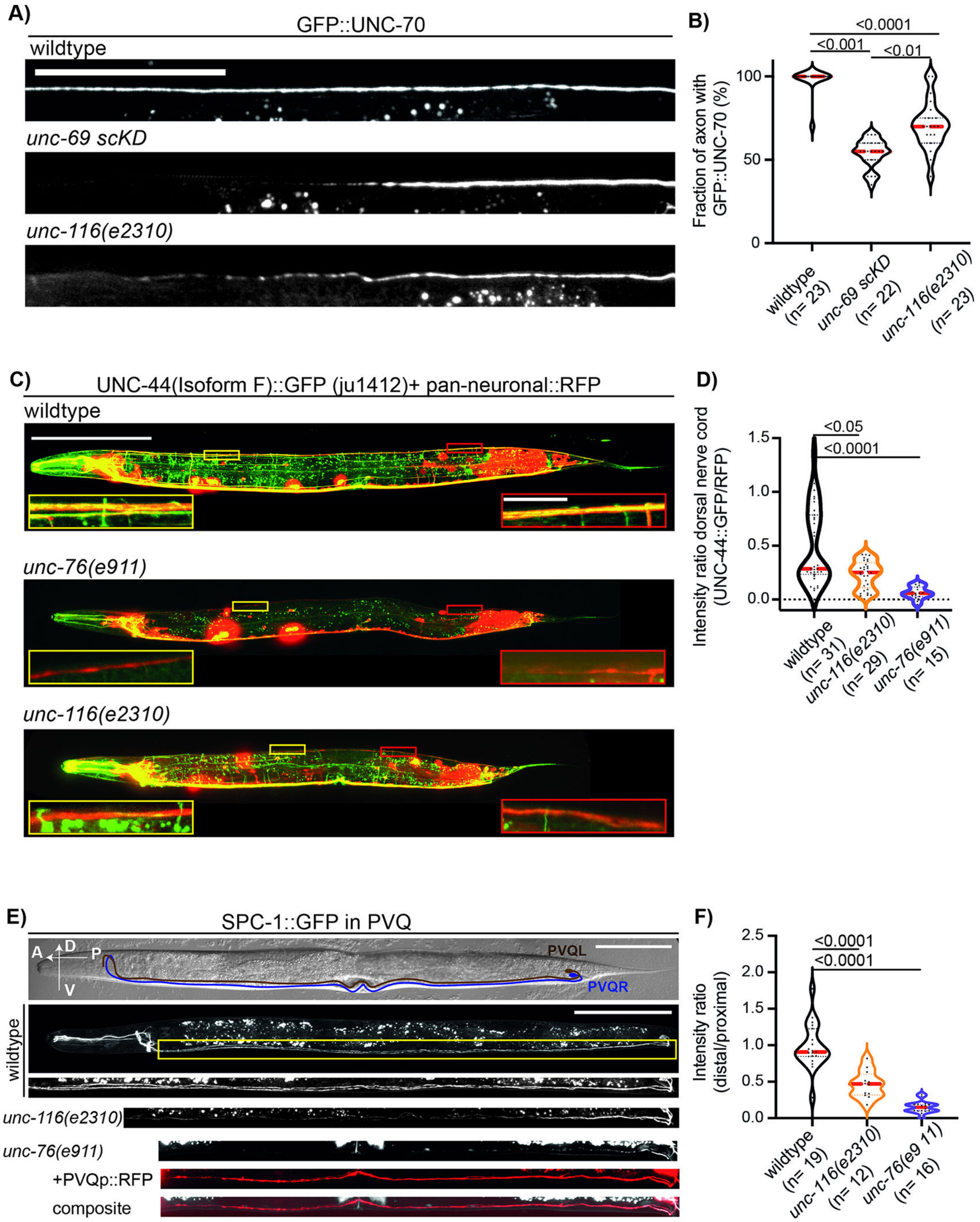

Figure 3: unc-76, unc-69 and unc-116 are required in different neurons for the distribution of proteins that can localize to the MPS.

A. UNC-70/ß-spectrin, endogenously tagged with 7xspGFP11, is lost from the distal DA9 axon in *unc-116(e2310)* and *unc-69 scKD* backgrounds. Scale: 50 µm. **B.** Quantification of A, Kruskal-Wallis test followed by Dunńs test for multiple comparisons. n= 22–23 animals per genotype **C.** Isoform F of UNC-44/Ankyrin was visualized in the entire animal by a GFP inserted in this specific isoform (ju1412), along with pan-neuronal RFP. *Unc-76(e911)* and *unc-116(e2310)* mutants show reduced UNC-44, including in regions where the DA9 axon is present (red insets) or elsewhere (yellow insets). Scale: 100 µm. **D.** Quantification of C. UNC-44(isoform F)::GFP signal was normalized to the RFP. Kruskal-Wallis test followed by an uncorrected Dunńs test. n= 15–31 animals per genotype. **E.** SPC-1::GFP localization is disrupted in PVQ neurons of *unc-76(e911)* and *unc-116(e2310*) animals. Schematic of PVQR and PVQL neurons is shown in the top panel. RFP marks the presence of the neuron and correct neuronal morphology in *unc-76 (e911*) mutants. Yellow boxed areas below main figures show a magnification of the distal axon. Scale:100 µm. **F.** SPC-1::GFP distribution is quantified as a ratio of signal intensity in the distal 50% of the axon to the proximal 50%. 1-way ANOVA followed by Tukeýs post-test for multiple comparisons. n= 12–19 animals per genotype.

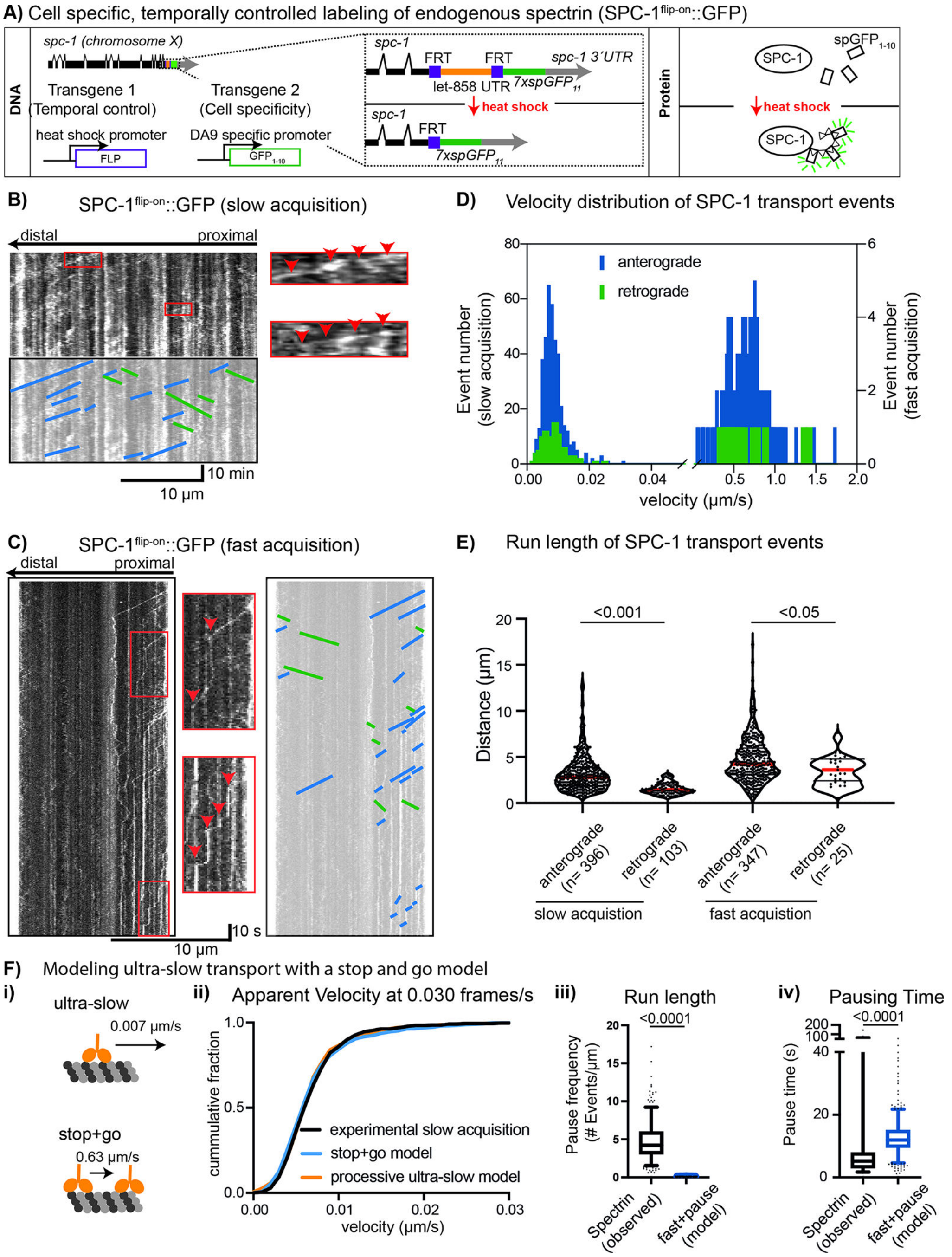

Figure 4: Bimodal slow axonal transport of α-spectrin.

A. Labelling strategy for single cell pulse labeling of endogenous α-spectrin (SPC-1flip-on::GFP). Heat shock drives expression of a recombinase that enables spectrin labeling by removing a STOP cassette. **B.** Representative kymograph showing ultra-slow movement of α-spectrin (SPC-1flip-on::GFP, 8–14 hours after induction) in the axon. Individual events are highlighted by boxes, in which red arrowheads point to the trace of the movement event. Acquisition rate: 30 s/ frame. Bottom panel highlights movement events in blue (anterograde) and green (retrograde). **C.** Representative kymograph showing stop-and-go transport of spectrin. Individual events are highlighted by boxes, pausing is indicated by red arrowheads. Acquisition rate: 0.3 s / frame. **D.** Velocity distribution of SPC-1$^{\text{flip-on}}$::GFP showing two distinct transport rates collected from n=13 (slow acquisition) and n= 20 (fast acquisition). **E.** Run length analysis of SPC-1$^{\text{flip-on}}$::GFP showing that the ultra-slow movement of spectrin is processive. Data in B+D were collected from n= 13 (slow acquisition) and n= 20 (fast acquisition) animals. Kruskal-Wallis test, followed by Dunńs post-test for multiple comparisons. **F.** Monte-Carlo simulations and modeling were used to generate apparent ultra-slow motility with the speed of individual runs corresponding to the speed of spectrin runs measured at high acquisition rate. Although this is theoretically possible (cumulative distribution plot, Fi), the run-length (Fii) and pause duration (Fiii) that are needed to generate apparent slow motility are inconsistent with the observed run-length and pause duration of spectrin. Statistics are based on Kruskal Wallis followed by Dunńs multiple comparison.

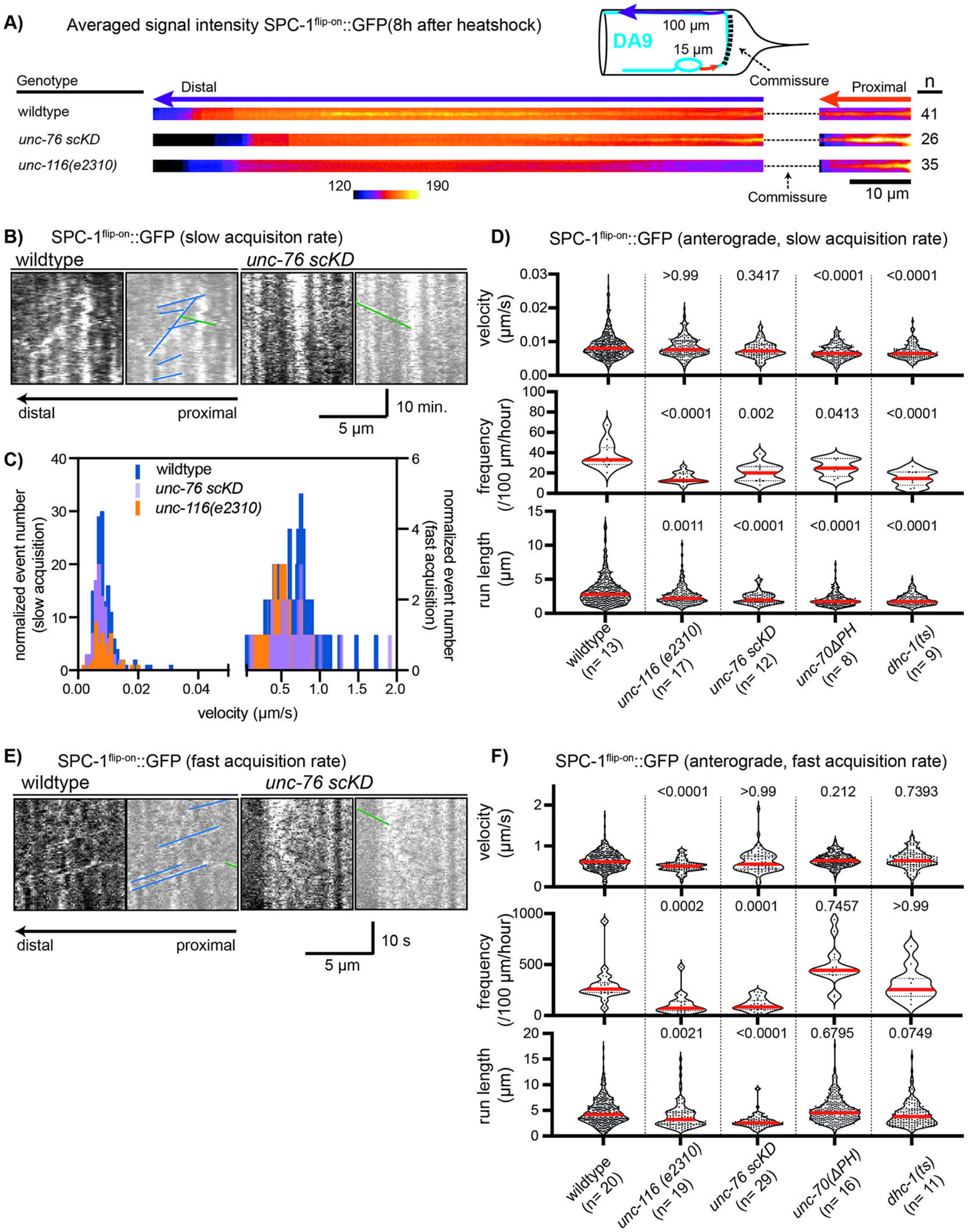

Figure 5: Spectrin transport requires *unc-116, unc-76, dhc-1* and the PH domain of UNC-70.

A. Averaged pseudo-colored line scans of SPC-$1^{\text{flip-on}}$::GFP at 8 hours after induction from animals of the indicated genotypes. Note proximal shift in the distribution of newly synthesized spectrin in *unc-116* mutants and *unc-76 scKD*. **B, D**. Representative kymographs (B) and quantifications (D) of SPC-$1^{\text{flip-on}}$::GFP (8–14 hours after induction) transport parameters under slow acquisitions in anterograde direction in the indicated genotypes (see Table S1 for retrograde events). Statistics are based on 1-way ANOVA followed by Tukeýs post-test for multiple comparisons (run length) or Kruskal-Wallis followed by Dunńs post-test for multiple comparisons (speed and frequency), p values (compared to wildtype) are indicated on plot. n= 9–17 animals per genotype as indicated below graph. **C.** SPC-1 transport velocity distribution in wildtype and mutants. **E, F.** Similar to B and C, except for the use of faster acquisition rates to reveal “stop-and-go” spectrin motility. Kruskal-Wallis followed by Dunńs post-test for multiple comparisons, p values of comparisons to wildtype are indicated on graph. N= 11–29 animals per genotype.

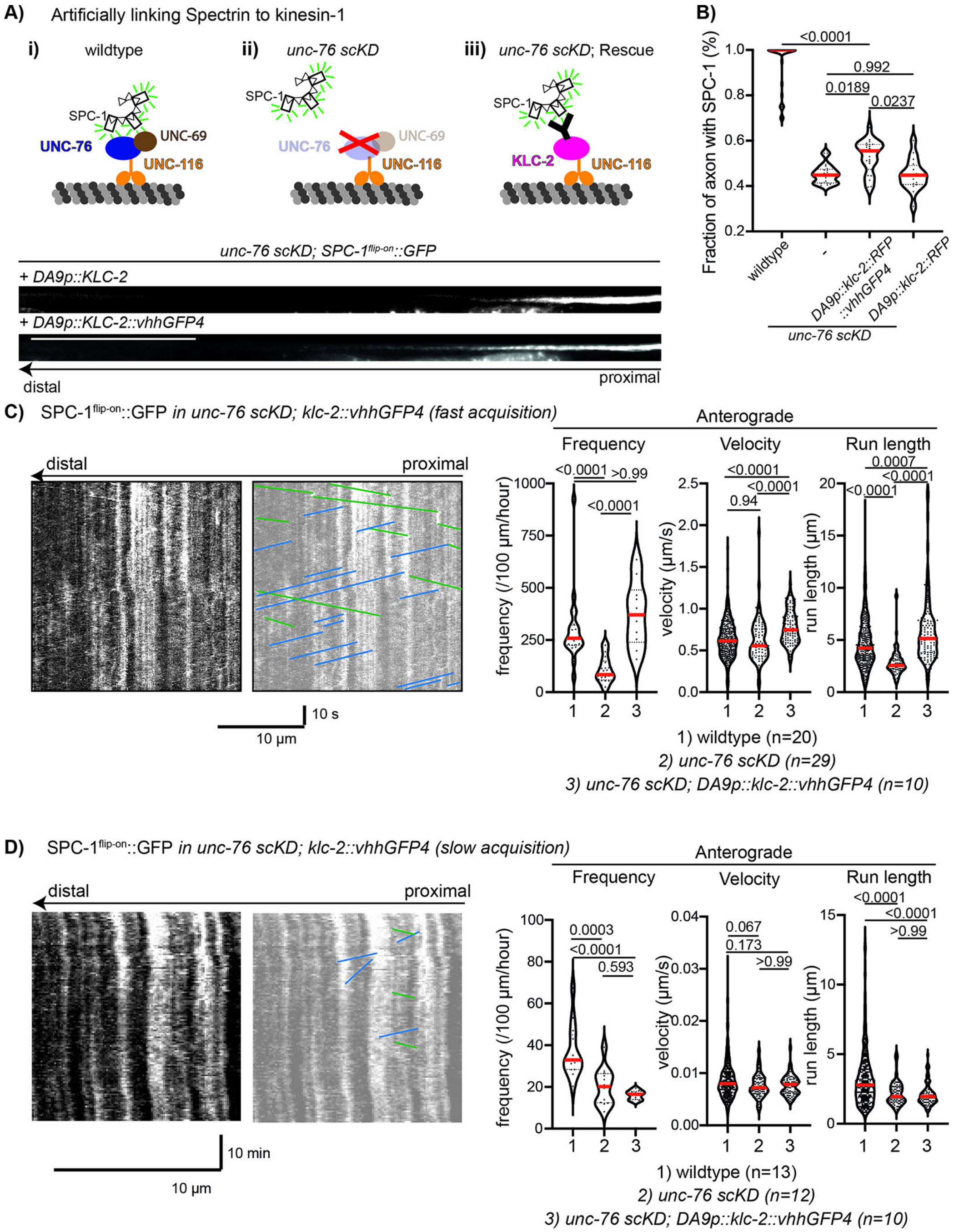

Figure 6: Restoring fast spectrin motility to *unc-76* mutants is not sufficient for fully restoring spectrin distribution to the distal axon.

A. Schematics of the strategy to restore spectrin motility in *unc-76 scKD* animals by linking it to kinesin light chain via a GFP nanobody (upper panels). Lower panels show representative images of control and rescue constructs. **B.** Quantification of results from (A), n= 16–39 animals per genotype, 1-way ANOVA followed by Tukeýs post-test for multiple comparisons. **C, D.** Representative kymographs and quantifications of spectrin transport events captured at 3 frames /s (C) or 0.03 frames /s (D, for ultra-slow motility). Artificially linking spectrin to kinesin generates robust bidirectional fast motility but not ultra-slow motility. Statistics based on Kruskal-Wallis test followed by Dunńs multiple comparison test, except for ultra-slow transport event frequency, which is 1-way ANOVA followed by Tukeýs multiple comparison. N= 10–29 animals per genotype (fast acquisition) and 10–13 animals per genotype (slow acquisition).

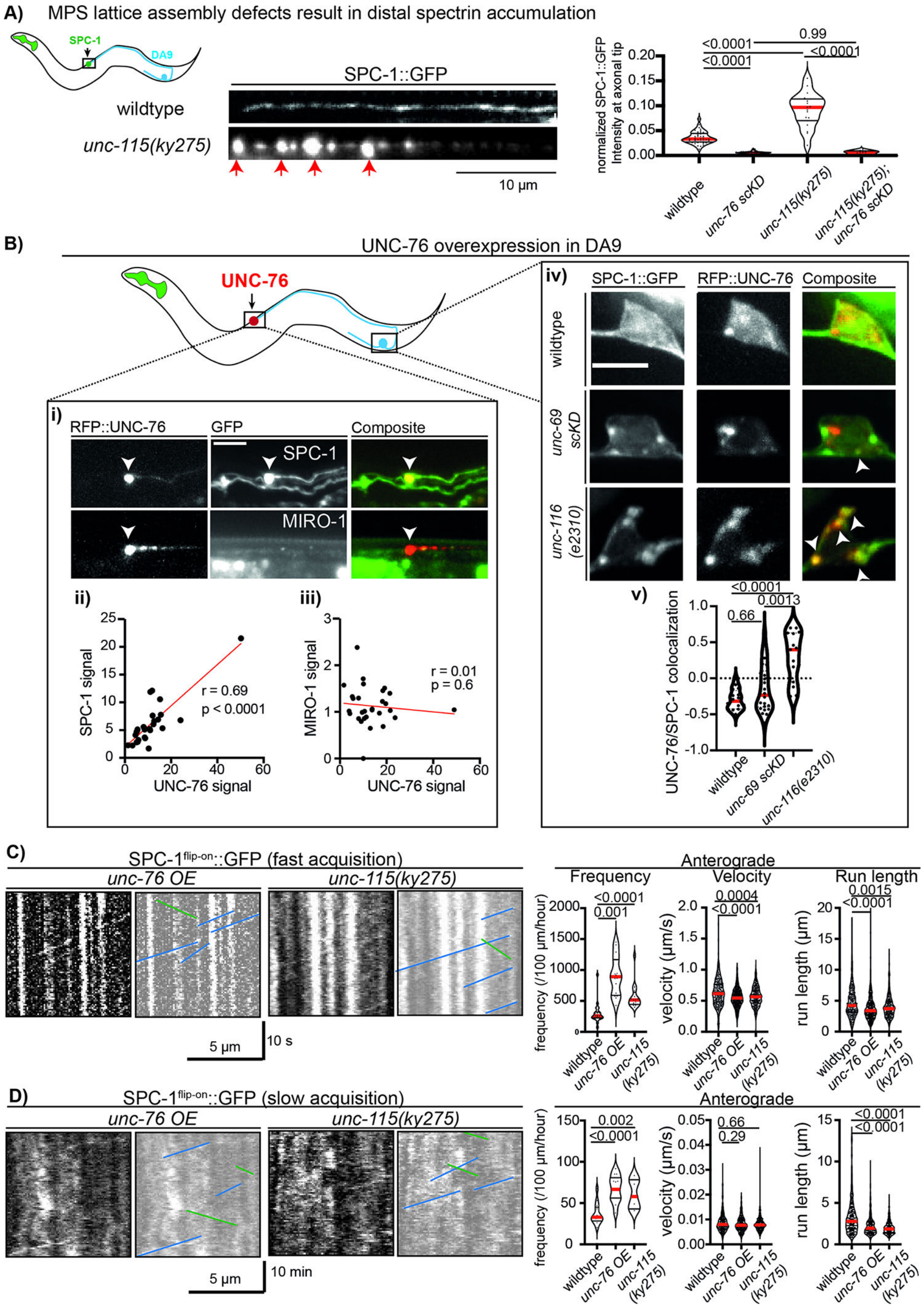

Figure 7: Overexpression of UNC-76 or MPS destabilization in *unc-115* mutants results in enhanced spectrin transport and its accumulation in the distal axon.

A. Representative images of SPC-1 in wildtype and *unc-115(ky275)* mutants in the distal axon. Scale: 10 µm. Right panel shows the quantification of the distal accumulation of SPC-1::GFP in the indicated genotypes. n= 14–39 animals per genotype, 1-way ANOVA followed by Tukeýs multiple comparisons. Single cell knockdown of UNC-76 suppresses the accumulation in *unc-115 (ky275)* mutants. **B.** Overexpression of UNC-76::RFP instructs spectrin localization to the tip of the axon. i) Representative images of overexpressed

RFP::UNC-76 with SPC-1::GFP or with a control kinesin-1 cargo (MIRO-1::GFP labels mitochondria) at the axon tip. Scale:10 µm. Bottom: linear regression of RFP::UNC-76 and SPC-1::GFP (ii, n = 28) or MIRO-1::GFP (iii, n = 29). iv) SPC-1 colocalizes with RFP::UNC-76 (white arrowheads) in the cell bodies of *unc-116* mutants and *unc-69 scKD*. v) Quantification of the colocalization in (iv) using Pearson correlation coefficient, n= 15–26 animals. **C, D.** Representative kymographs and quantifications of SPC-1$^{\text{flip-on}}$::GFP transport under fast and slow acquisition rates show enhanced motility in UNC-76 overexpression conditions and *unc-115 (ky275)* mutants. n= 7–20 animals per condition. Kruskal-Wallis followed by Dunńs multiple comparison for statistics.

Key resources table

REAGENT or RESOURCE	**SOURCE**	**IDENTIFIER**
Antibodies		
anti-GFP (goat) peroxidase conjugated	Rockland	600-103-215
anti-RFP (Rabbit)	Rockland	600-401-379
anti-HaloTag (Rabbit)	Promega	G9211
anti-Rabbit HRP-conjugated secondary antibody 1:3000	Cell signaling	7074S
monoclonal anti-beta-tubulin antibody	Sigma	T5201
Bacterial and virus strains		
Escherichia coli: OP50 Strain	Caenorhabditis Genetics Center (CGC)	OP50
Escherichia coli: DH10B, chemical competent cells	Thermo Fisher	18297010
Chemicals, peptides, and recombinant proteins		
S. pyogenes Cas9 3NLS, 10µg/µl	IDT	Cat# 1081058
Auxin	Alfa Aesar	A10556
Casein	Sigma	C5890
Taxol (Paxitaxel)	Cytoskeleton	TXD01
AMP-PNP	Sigma	A2647
SuperSignal™ West Pico PLUS Chemiluminescent Substrate	Thermo Fisher Scientific	34579
SuperSignal™ West Femto Maximum Sensitivity Substrate	Thermo Fisher Scientific	34094
GFP-trap agarose beads	Chromotek	gta
Critical commercial assays		
EnGen sgRNA Synthesis Kit, S. pygenes	NEB	E3322S
Experimental models: Cell lines		
HEK293T	ATCC	CB_12022001
COS7	ATCC	**CRL-1651**
Experimental models: Organisms/strains		
unc-70(syb1684[unc-70(1166R + AID + 1167D)]) (V)	This study.	phx1684
miro-1(wp119[7xGFP$_{11}$::miro-1]) (IV), shyIs36 [Pmig-13::GFP1-10, Podr-1::RFP] (V)	This study, wp119 has been generated by the Hammarlund lab, Youjun Wu, Yale School of Medicine, Departments for Neuroscience and Genetics	MTS1291
oxTi185[ttTi5605 + NeoR(+) + unc-18(+)] (I), unc-119(ed3) (III)	C. Frøkjær-Jensen, Jorgensen Lab, School of Biological Science, University of Utah	EG8078
unc-44(ju1412[unc-44::GFP]) (IV)	Fei Chen, Jin Lab, UCSD, School of Biological Sciences, ordered through CGC	CZ24990
spc-1(cas1047[spc-1::7×GFP11]) (X); wpIs141[Psra-6::GFP1-10, Pmyo-2::mCherry] (II)	This study	MTS742
spc-1(cas1047[spc-1::7×GFP11]) (X); shyEx155[Pmig-13::GFP1-10, Podr-1::RFP]	This study	MTS743
spc-1(cas1047[spc-1::7×GFP11]) (X); shyIs35[Pmig-13::GFP1-10, Podr-1::RFP] (IV)	This study	MTS826

REAGENT or RESOURCE	**SOURCE**	**IDENTIFIER**
spc-1(cas1047[spc-1::7×GFP11]) (X); shyIs36[Pmig-13::GFP1-10, Podr-1::RFP] (V)	This study	MTS879
spc-1 (shy84 [spc-1::FRT::let-858UTR::FRT::7xgfp11]) (X); shySi4 [(hsp16.4p::FLP, unc-119(+))*oxTi185] (I); shyIs35[Pmig-13::GFP1-10, Podr-1::RFP] (IV)	This study	MTS1082
spc-1 (shy84 [spc-1::FRT::let-858UTR::FRT::7xgfp11]) (X); shySi4 [(hsp16.4p::FLP, unc-119(+))*oxTi185] (I); shyIs36[Pmig-13::GFP1-10, Podr-1::RFP] (V)	This study	MTS1067
spc-1(cas1047[spc-1::7×GFP11]) (X); shyIs36[Pmig-13::GFP1-10, Podr-1::RFP] (V); shyEx305[Pmig-13::TIR1, Podr-1::RFP]; unc-70(syb1684[unc-70(1166R + AID + 1167D)]) (V)	This study	MTS1006
unc-70(shy112 [7xGFP11::unc-70]) (V); shyIs36[Pmig-13::GFP1-10, Podr-1::RFP] (V)	This study	MTS1510
unc-70(shy112 [7xGFP11::unc-70]) (V); shyIs36 (V); spc-1(shy111[spc-1::aid]) (X); shyIs53[Pmig-13::TIR1, Podr-1::RFP] (II)	This study	MTS1515
unc-116(e2310) (III); spc-1(cas1047[spc-1::7×GFP11]) (X); shyIs35 [Pmig-13::GFP1-10, Podr-1::RFP] (IV)	This study	MTS953
unc-116(e2310) (III); shyEx369[Pmig-13::unc-116::SL2::mCherry, Podr-1::GFP]; spc-1(cas1047[spc-1::7×GFP11]) (X); shyIs35 [Pmig-13::GFP1-10, Podr-1::RFP] (IV)	This study	MTS1360
unc-116 (shy92 [unc-116::AID]) (III); shyEx305[Pmig-13::TIR1, Podr-1::RFP]; spc-1(cas1047[spc-1::7×GFP11]) (X); shyIs35[Pmig-13::GFP1-10, Podr-1::RFP] (IV)	This study	MTS1489
unc-116(rh24sb79) (III); spc-1(cas1047[spc-1::7×GFP11]) (X); shyIs35 (IV)	This study	MTS954
unc-76(shy19[zf-1::unc-76]) (V); shyIS16 [Pmig-13::ZF-1, Pttx-3::RFP] (V); spc-1(cas1047[spc-1::7×GFP11]) (X); shyIs35 [Pmig-13::GFP1-10, Podr-1::RFP] (IV)	This study	MTS951
spc-1(cas1047[spc-1::7×GFP11]) (X); shyIs35 [Pmig-13::GFP1-10, Podr-1::RFP] (IV); shyEx78[Pmig-13::FEZ1, Pmig-13::STOP::RFP::Podr-1::GFP] ; unc-76 (shy19[zf-1::unc-76]) (V); shyIs16[Pmig-13::ZF-1, Pttx-3::RFP] (V)	This study	MTS1003
unc-69(syb2774[unc-69::zf-1::7xGFP11])(III); shyIs9[Pmig-13::ZF-1, Pttx-3::RFP] (IV); spc-1(cas1047[spc-1::7×GFP11]) (X); shyIs36[Pmig-13::GFP1-10, Podr-1::RFP](V)	This study	MTS1337
unc-69(syb2774[unc-69::zf-1::7xGFP11])(III); shyIs9 [Pmig-13::ZF-1, Pttx-3::RFP] (IV); spc-1(cas1047[spc-1::7×GFP11]) (X); shyIs36[Pmig-13::GFP1-10, Podr-1::RFP](V); shyEx381[Pmig-13::SCOC, Podr-1::GFP]	This study	MTS1433
spc-1(cas1047[spc-1::7×GFP11]) (X), shyEx155[Pmig-13::GFP1-10, Podr-1::RFP]; unc-76(shy19[zf-1::unc-76]) (V); shyIs16[Pmig-13::ZF-1, Pttx-3::RFP] (V);unc-69(syb2774[unc-69::zf-1::7xGFP11])(III)	This study	MTS877
unc-116(e2310) (III); unc-76(shy19[zf-1::unc-76]) (V);shyIs16[Pmig-13::ZF-1, Pttx-3::RFP] (V); spc-1(cas1047[spc-1::7×GFP11]) (X); shyEx155[Pmig-13::GFP1-10, Podr-1::RFP]	This study	MTS813
spc-1(cas1047[spc-1::7×GFP11]) (X); shyIs35 [Pmig-13::GFP1-10, Podr-1::RFP] (IV); *jip-1(gk133506)* (II)	This study	MTS1484
spc-1(cas1047[spc-1::7×GFP11]) (X); shyIs35 [Pmig-13::GFP1-10, Podr-1::RFP] (IV); *unc-16(ce483)* (III)	This study	MTS1290
klc-2(km11), klc-1(ok2609), spc-1(cas1047[spc-1::7×GFP11]) (X), shyEx155[Pmig-13::GFP1-10, Podr-1::RFP]	This study	MTS827
unc-104(e1265); spc-1(cas1047[spc-1::7×GFP11]) (X); shyIs35 [Pmig-13::GFP1-10, Podr-1::RFP] (IV)	This study	MTS906
spc-1 (shy84 [spc-1::FRT::let-858UTR::FRT::7xgfp11]) (X); shySi4 [(hsp16.4p::FLP, unc-119(+))*oxTi185] (I); shyIs35 [Pmig-13::GFP1-10, Podr-1::RFP] (IV); unc-76(shy19[zf-1::unc-76])(V); shyIs16[Pmig-13::ZF-1, Pttx-3::RFP] (V)	This study	MTS1167
spc-1 (shy84 [spc-1::FRT::let-858UTR::FRT::7xgfp11]) (X); shySi4 [(hsp16.4p::FLP, unc-119(+))*oxTi185] (I); shyIs35[Pmig-13::GFP1-10, Podr-1::RFP] (IV), unc-116(e2310) (III)	This study	MTS1168
unc-116(e2310); unc-70(shy112 [7xGFP11::unc-70]) (V); shyIs36[Pmig-13::GFP1-10, Podr-1::RFP] (V)	This study	MTS1516
unc-69(syb2774[zf-1::7xGFP11::unc-69])(III); shyIs9[Pmig-13::ZIF-1, Pttx-3::RFP] (IV); unc-70(shy112 [7xGFP11::unc-70]) (V), shyIs36[Pmig-13::GFP1-10, Podr-1::RFP] (V)	This study	MTS1535
unc-44 (ju1412[unc-44::GFP]) (IV); shyEx415[Prab-3::RFP, Punc-122::RFP]	This study	MTS1688

REAGENT or RESOURCE	**SOURCE**	**IDENTIFIER**
unc-44 (ju1412[unc-44::GFP]) (IV); shyEx415[Prab-3::RFP, Punc-122::RFP]; unc-116(e2310) (III)	This study	MTS1689
unc-44 (ju1412[unc-44::GFP]) (IV); shyEx415[Prab-3::RFP, Punc-122::RFP]; unc-76(e911) (V)	This study	MTS1693
spc-1(cas1047[spc-1::7×GFP11]) (X); wpIs141[Psra-6::GFP1-10, Pmyo-2::mCherry] (II); unc-76(e911)(V); shyEx396[Psra-6::tagRFP, Podr-1::GFP]	This study	MTS1462
spc-1(cas1047[spc-1::7×GFP11]) (X); wpIs141[Psra-6::GFP1-10, Pmyo-2::mCherry] (II); unc-116(e2310) (III)	This study	MTS1517
shyEx268[Pmig-13::GFP::RAB11.1, Podr-1::RFP]	This study	MTS1049
unc-76 (shy19[zf-1::unc-76])(V); shyIs16 [Pmig-13::ZF-1, Pttx-3::RFP] (V); shyEx268[Pmig-13::GFP::RAB11.1, Podr-1::RFP]	This study	MTS1197
unc-116(e2310); shyEx268[Pmig-13::GFP::RAB11.1, Podr-1::RFP]	This study	MTS1306
tba-1(ok1135) (I); wySi256/+ [Punc-4C::CRE, Punc-122::RFP] (II); him-8 (IV); wyIs463[Pmig-13::STOP::GFP::TBA-1], shyIs16 [Pmig-13::ZF-1, Pttx-3::RFP] (V), unc-76(shy19[zf-1::unc-76])(V); wyEx2709	This study	MTS1303
unc-76(shy45[10xGFP11::unc-76]) (V); shyEx155 [Pmig-13::GFP1-10, Podr-1::RFP]	This study	MTS598
unc-116(e2310) (III); unc-76(shy45[10xGFP11::unc-76]) (V); shyEx155 [Pmig-13::GFP1-10, Podr-1::RFP]	This study	MTS652
unc-69(syb2774[zf-1::7xGFP11::unc-69])(III); unc-76(shy45[10xGFP11::unc-76]) (V); shyEx155 [Pmig-13::GFP1-10, Podr-1::RFP]	This study	MTS1071
unc-69(syb2774[zf-1::7xGFP11::unc-69]) (III) ; shyEx155 [Pmig-13::GFP1-10, Podr-1::RFP]	This study	MTS839
unc-69(syb2774[zf-1::7xGFP11::unc-69])(III); *unc-76(e911)* (V); shyEx155 [Pmig-13::GFP1-10, Podr-1::RFP]	This study	MTS1072
unc-76(shy19[zf-1::unc-76]) (V); shyIS16[Pmig-13::ZF-1, Pttx-3::RFP] (V); spc-1(cas1047[spc-1::7×GFP11]) (X); shyIs35[Pmig-13::GFP1-10, Podr-1::RFP] (IV); shyEx370[Pmig-13::KLC-2(IsoformA)::tagRFP::vhhGFP4, Podr-1::GFP]	This study	MTS1361
unc-76(shy19[zf-1::unc-76]) (V); shyIS16[Pmig-13::ZF-1, Pttx-3::RFP] (V); spc-1(cas1047[spc-1::7×GFP11]) (X); shyIs35[Pmig-13::GFP1-10, Podr-1::RFP] (IV); shyEx380[Pmig-13::KLC-2(IsoformA)::tagRFP, Podr-1::GFP]	This study	MTS1420
spc-1(cas1047[spc-1::7×GFP11]) (X); shyIs35[Pmig-13::GFP1-10, Podr-1::RFP] (IV); shyEx336[Pmig-13::tagRFP::UNC-76(IsoformA), Podr-1::GFP]	This study	MTS1256
shyEx336[Pmig-13::tagRFP::UNC-76(IsoformA), Podr-1::GFP]; miro-1(wp119[7xGFP$_{11}$::miro-1) (IV); shyIS36 (V)	This study	MTS1413
spc-1(cas1047[spc-1::7×GFP11]) (X); shyIs35[Pmig-13::GFP1-10, Podr-1::RFP] (IV); shyEx336[Pmig-13::tagRFP::UNC-76(IsoformA), Podr-1::GFP]; unc-116(e2310) (III)	This study	MTS1665
unc-69(syb2774[zf-1::7xGFP11::unc-69]) (III); shyIs9[Pmig-13::ZF-1, Pttx-3::RFP] (IV); spc-1(cas1047[spc-1::7×GFP11]) (X); shyIs36[Pmig-13::GFP1-10, Podr-1::RFP](V); shyEx336[Pmig-13::tagRFP::UNC-76(IsoformA), Podr-1::GFP]	This study	MTS1710
dhc-1(shy179(H2159L)) (I); spc-1 (shy84 [spc-1::FRT::let-858UTR::FRT::7xgfp11]) (X); shySi4 [(hsp16.4p::FLP, unc-119(+))*oxTi185] (I); shyIs36[Pmig-13::GFP1-10, Podr-1::RFP] (V)	This study	MTS2148
spc-1(cas1047[spc-1::7×GFP11]) (X); shyIs40[Pitr-1::GFP1-10, Podr-1::RFP] (I)	This study	MTS1720
spc-1(cas1047[spc-1::7×GFP11]) (X); shyIs40[Pitr-1::GFP1-10, Podr-1::RFP] (I), unc-115(ky275) (X)	This study	MTS1729
spc-1(cas1047[spc-1::7×GFP11]) (X); shyIs40[Pitr-1::GFP1-10, Podr-1::RFP] (I), unc-115(shy159[M1STOP]) (X)	This study	MTS2212
spc-1(cas1047[spc-1::7×GFP11]) (X); shyIs35[Pmig-13::GFP1-10, Podr-1::RFP] (I), unc-115(ky275) (X)	This study	MTS2250
spc-1(cas1047[spc-1::7×GFP11]) (X); shyIs35[Pmig-13::GFP1-10, Podr-1::RFP] (I), unc-115(ky275) (X); unc-76 (shy19[zf-1::unc-76])(V); shyIs16 [Pmig-13::ZF-1, Pttx-3::RFP] (V)	This study	MTS2249

REAGENT or RESOURCE	**SOURCE**	**IDENTIFIER**
spc-1(cas1047[spc-1::7×GFP11]) (X); shyIs83[Pmec-17::GFP1-10] (I)	This study	MTS2000
spc-1(cas1047[spc-1::7×GFP11]) (X); shyIs83[Pmec-17::GFP1-10] (I); unc-115(ky275) (X)	This study	MTS2251
spc-1(cas1047[spc-1::7×GFP11]) (X); shyIs83[Pmec-17::GFP1-10] (I); unc-70(syb1684[unc-70(1166R + AID + 1167D)]) (V); shyEx517[Pmec-17::tir1]	This study	MTS2093
spc-1(cas1047[spc-1::7×GFP11]) (X); shyIs83[Pmec-17::GFP1-10] (I); unc-76 (shy19[zf-1::unc-76])(V); shyEx536[Pmec-17::ZIF-1]	This study	MTS2154
unc-115(shy161[3xGFP11::unc-115]) (X); shyIs83[Pmec-17::GFP1-10] (I)	This study	MTS2215
spc-1 (shy84 [spc-1::FRT::let-858UTR::FRT::7xgfp11]) (X); shySi4 [(hsp16.4p::FLP, unc-119(+))*oxTi185] (I); shyIs36[Pmig-13::GFP1-10, Podr-1::RFP] (V); shyEx540 [Pmig-13::UNC-76]	This study	MTS2226
spc-1 (shy84 [spc-1::FRT::let-858UTR::FRT::7xgfp11]) (X); shySi4 [(hsp16.4p::FLP, unc-119(+))*oxTi185] (I); shyIs36[Pmig-13::GFP1-10, Podr-1::RFP] (V); unc-76 (shy19[zf-1::unc-76])(V); shyIs16[Pmig-13::ZF-1, Pttx-3::RFP] (V); shyEx548[Pmig-13::KLC-2::vhhGFP4]	This study	MTS2290
Oligonucleotides		
Oligonucleotides were ordered from SigmaAldrich. A list of all oligonucleotides used in this study is provided in supplemental table S2.	Sigma Aldrich	See table S2.
Single stranded oligonucleotides that were used as CRISPR repair templates were ordered from IDT and are also listed in table S3.	IDT	See table S3.
Recombinant DNA		
pRF4::rol-6(su1006)	Melo CC, Ambros Lab, UMass, Program in Molecular Medicine	pRF-4
Prab-3::mCherry::unc-54utr	C. Frøkjær-Jensen, Jorgensen Lab, School of Biological Science, University of Utah	pGH8
Phsp-16.4::FLP::let-858utr_pXF87 backbone	This study	pOVG19
Phsp-16.41:peel-1:tbb-2utr	C. Frøkjær-Jensen, Jorgensen Lab, School of Biological Science, University of Utah	pMA122
Pmyo-2::mCherry::unc-54utr	C. Frøkjær-Jensen, Jorgensen Lab, School of Biological Science, University of Utah	pCFJ90
Pmig-13::UNC-116::SL2::mCherry	This study	pOVG26
Pmig-13::tagRFP::UNC-76	This study	pOVG36
Pmig-13::KLC-2(isoformA)::tagRFP	This study	pOVG43
Pmig-13::KLC-2(isoformA)::tagRFP::vhhGFP4	This study	pOVG44
Pmig-13::SCOC	This study	pMR18
Pmig-13::FEZ1	This study	pMR20
Pmig-13::KLC-2(isoformA)::vhhGFP4	This study	pOVG63
Pmec-17::zif1	This study	pOVG67
Pmec-17::3xGFP	This study	pOVG70
Pmec-17::tir1	This study	pOVG65
Pmec-17::GFP$_{1-10}$	This study	pOVG56
Pmig-13::UNC-76	This study	pMR13

REAGENT or RESOURCE	**SOURCE**	**IDENTIFIER**
Pcmv::SPTBN1(Q01082-1)::eGFP	This study	pOVG40
Pcmv::HALO::SCOC	This study	pGLS5
Pcmv::mCherry::FEZ1	This study	pOVG46
Pcmv::SNAP::FEZ1	This study	pGLS25
Software and algorithms		
Prism Version 7	GraphPad	
Illustrator	Adobe	
RStudio	R	
Image J	NIH	
EndNote20	EndNote	
Algorithm: Spectrin-Axonal-Mobility-Model.	Generated by: Gramlich lab, Michael Gramlich, Auburn University, Physics department DOI: https://zenodo.org/badge/latestdoi/615469432	Code is available on github: https://github.com/AU-Neurophysics-Lab/Spectrin-Axonal-Mobility-Model.